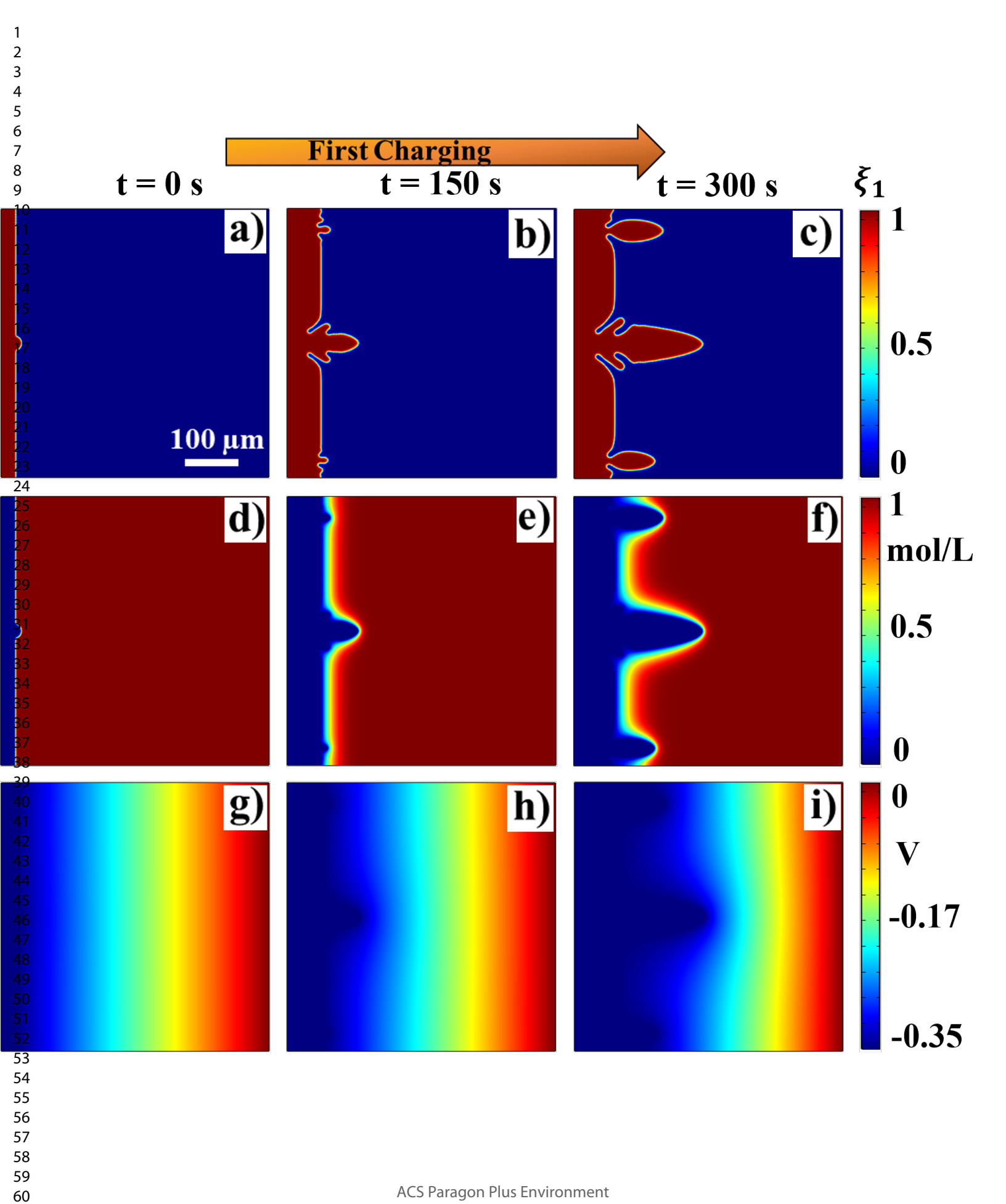
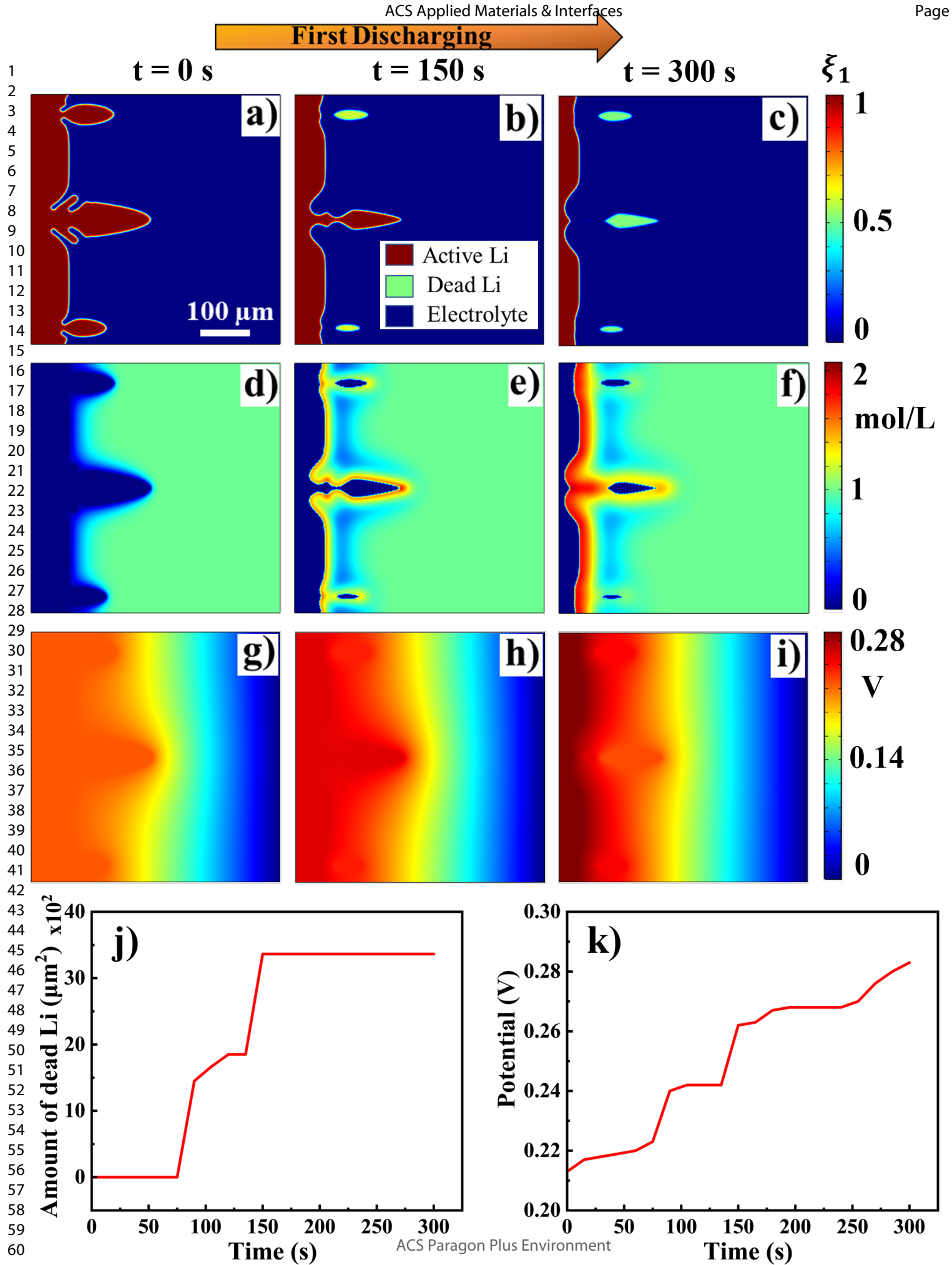
This document is confidential and is proprietary to the American Chemical Society and its authors. Do not copy or disclose without written permission. If you have received this item in error, notify the sender and delete all copies.

# Dendrite Growth and Dead Lithium Formation in Lithium Metal Batteries and Mitigation Using a Protective Layer: A Phase-Field Study

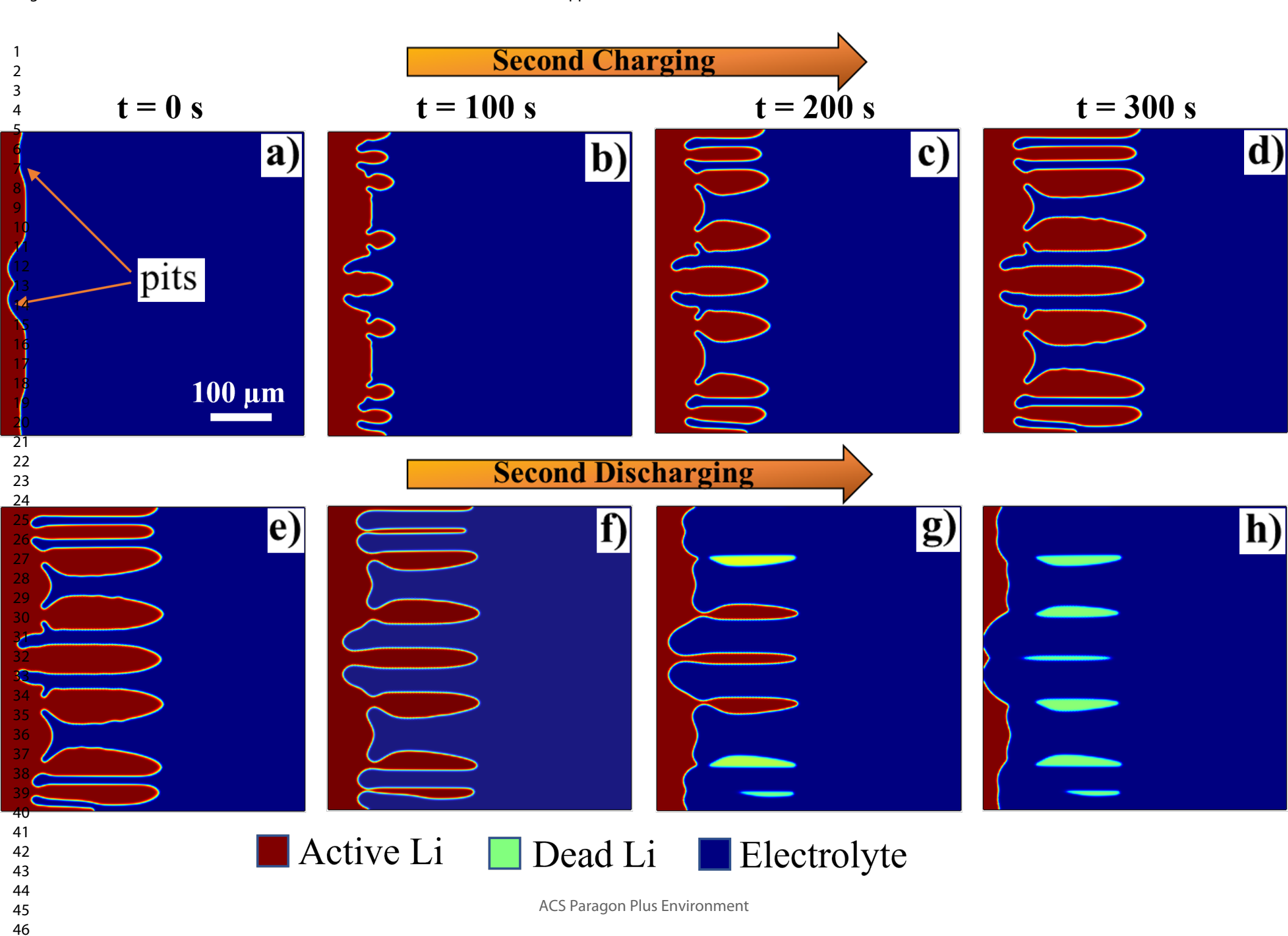
Journal:	ACS Applied Materials & Interfaces			
Manuscript ID	am-2024-08605g.R2			
Manuscript Type:	Article			
Date Submitted by the Author:	n/a			
Complete List of Authors:	Pant, Bharat; The University of Texas at Arlington, Materials Science and Engineering Ren, Yao; The University of Texas at Arlington, Materials Science and Engineering Cao, Ye; University of Texas at Arlington, Materials Science and Engineering			

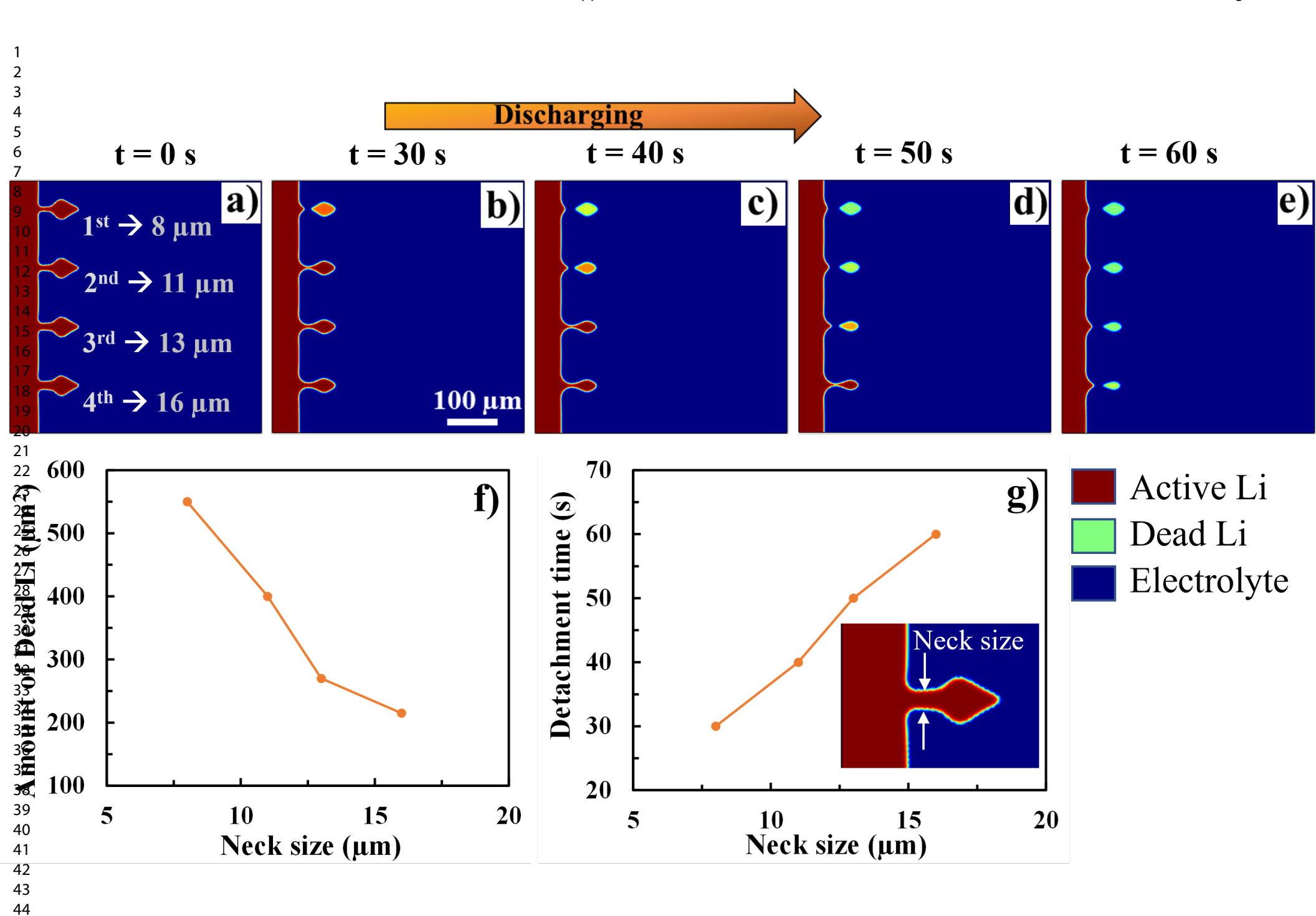
SCHOLARONE™ Manuscripts



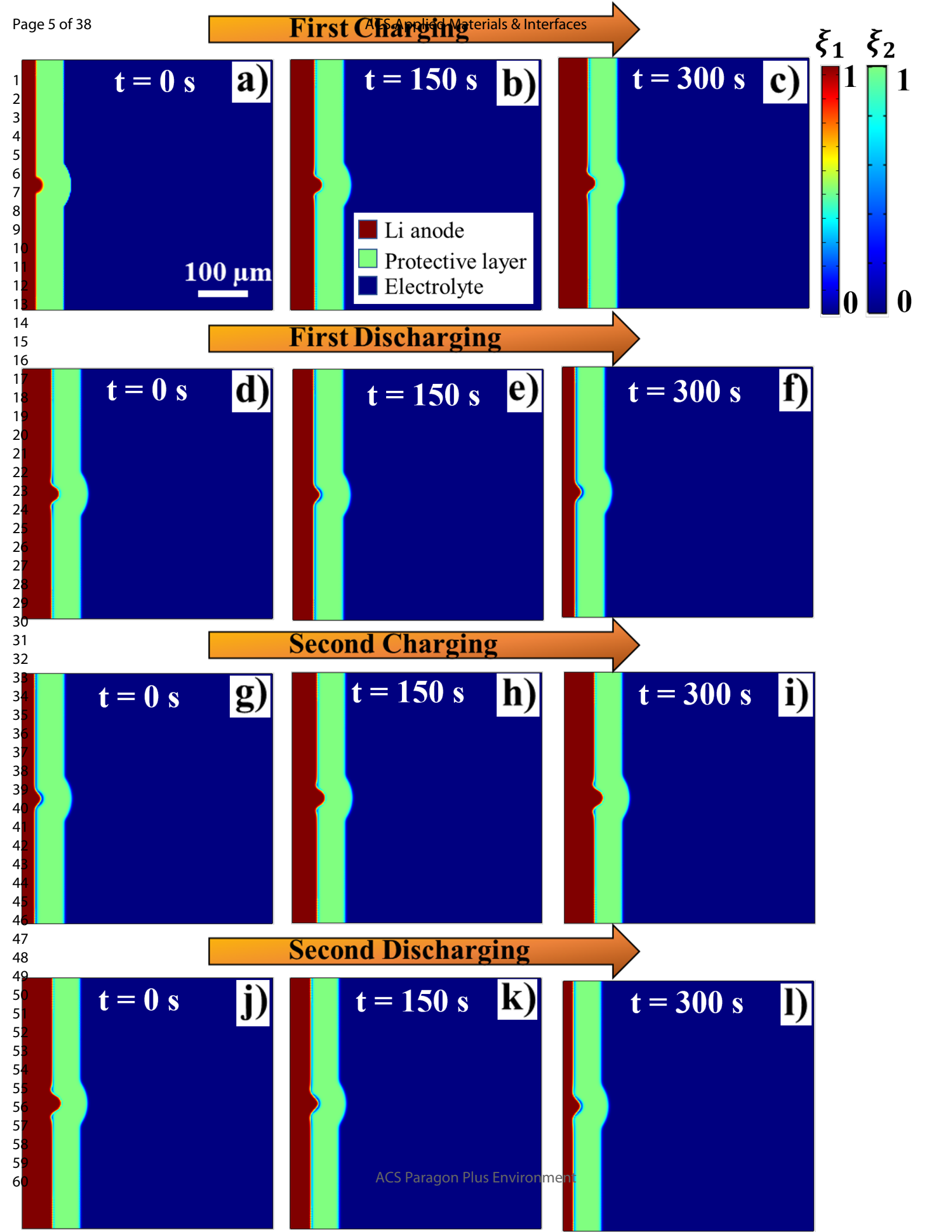


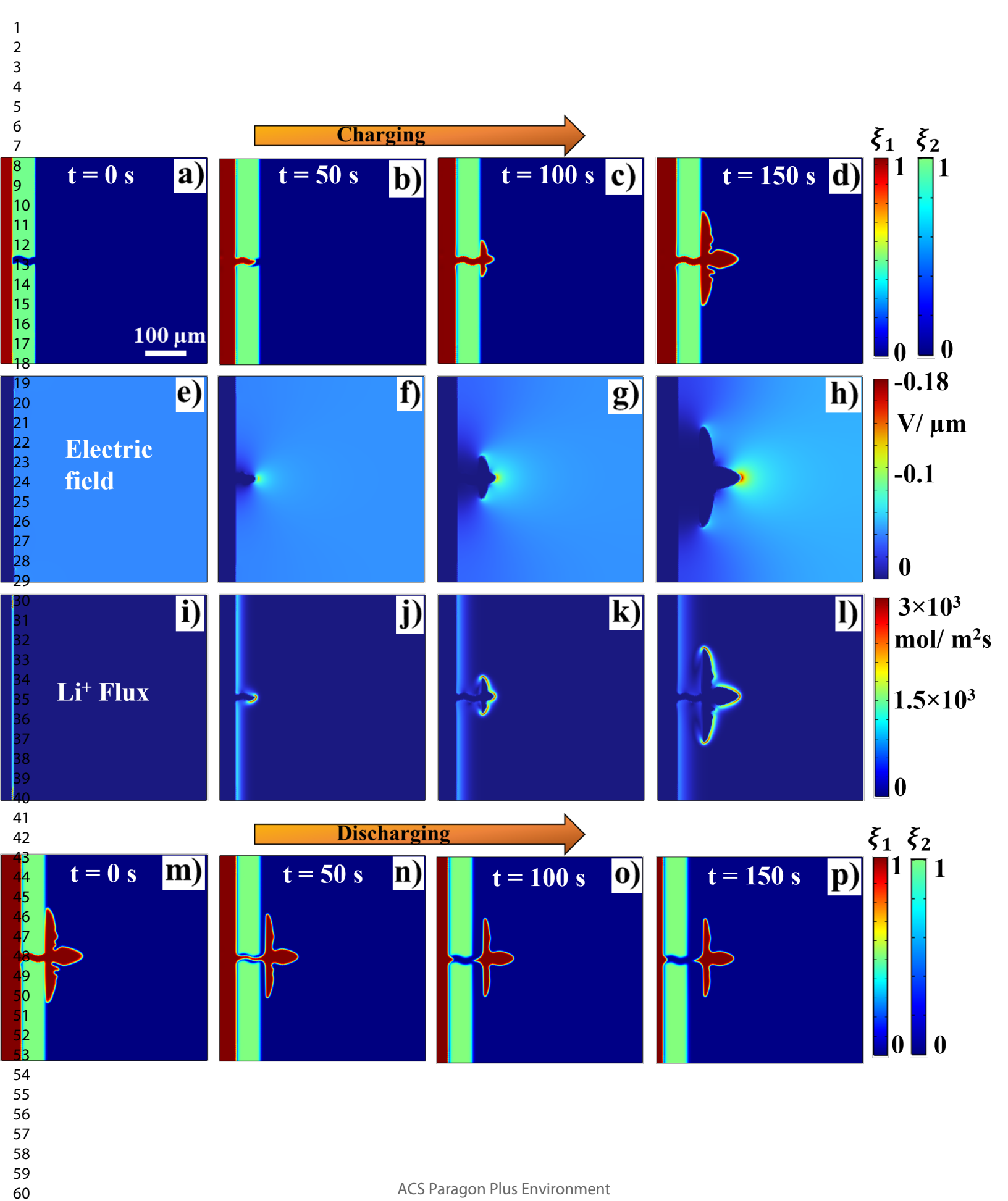
47





45 46 47





# Dendrite Growth and Dead Lithium Formation in Lithium Metal Batteries and Mitigation Using a Protective Layer: A Phase-Field Study

Bharat Raj Pant, 1 Yao Ren, 1 Ye Cao1,\*

<sup>1</sup>Department of Materials Science and Engineering, University of Texas at Arlington, Arlington, TX 76019

Corresponding author: Ye Cao

\*Email: ye.cao@uta.edu

Phone: +1 (817) 272-1858

Address: ELB 332, 501 W 1st St., Arlington, TX, 76019 USA

#### Abstract

Lithium metal batteries (LMBs) are considered one of the most promising next-generation rechargeable batteries due to their high specific capacity. However, severe dendrite growth and subsequent formation of dead lithium (Li) during battery cycling process impede its practical application. Although extensive experimental studies have been conducted to investigate the cycling process, and several theoretical models were developed to simulate the Li dendrite growth, there are limited theoretical studies on the dead Li formation, as well as the entire cycling process. Herein, we developed a phase-field model to simulate both the electroplating and stripping process in a bare Li anode and Li anode covered with a protective layer. A step function is introduced in the stripping model to capture the dynamics of dead Li. Our simulation clearly shows the growth of dendrites from bare Li anode during charging. These dendrites detach from the bulk anode during discharging, forming dead Li. Dendrite growth becomes more severe in subsequent cycles due to enhanced surface roughness of the Li anode, resulting in increasing amount of dead Li. In addition, it is revealed that dendrites with smaller base diameters detach faster at the base and produce more dead lithium. Meanwhile, the Li anode covered with a protective layer cycles smoothly without forming Li dendrite and dead Li. However, if the protective layer is fractured, Li metal preferentially grows into the crack due to enhanced Li-ion (Li<sup>+</sup>) flux and forms a dendrite structure after penetration through the protective layer, which accelerates the dead Li formation in the subsequent stripping process. Our work thus provides a fundamental understanding of the mechanism of dead Li formation during the charging/discharging process and sheds light on the importance of the protective layer in the prevention of dead Li in LMBs.

Keywords: Dead lithium, protective layer, phase-field simulation, dendrite growth, cycling.

#### 1. Introduction

Demand for lithium-ion batteries (LIBs) is growing due to an increase in the production of portable electronic devices and electric vehicles (EVs). 1 For decades, graphite has been extensively used as the primary anode material in traditional LIBs. Unfortunately, graphite has reached its theoretical limit due to its low specific energy capacity (372 mAhg<sup>-1</sup>) and is not suitable for highcapacity batteries. <sup>2</sup> The growing need for high-capacity batteries has prompted the search for alternative anode materials. <sup>3</sup> Over the past decades, lithium metal batteries (LMBs) have emerged as an alternative to LIBs due to the high specific capacity (3860 mAhg-1) and low redox potential of lithium metal (-3.04 V vs. standard hydrogen electrode) used as anode materials. <sup>3</sup> Nevertheless, severe dendrite growth during the cycling process impedes its practical application. <sup>2</sup> These dendrites reduce the Coulombic efficiency of the cell and cause safety issues due to shortcircuiting. <sup>4</sup> Additionally, during discharging the dendrites can easily lose the structural connection to the bulk anode and form dead Li, which no longer participates in the subsequent chargingdischarging process, causing irreversible capacity loss. <sup>5</sup> The continuous formation and subsequent pile-up of dead Li during each cycle may build a thick layer of dead Li on the lithium surface, hindering the transport of Li ions (Li<sup>+</sup>) from electrolyte to electrode. <sup>6,7</sup>

Several experimental studies have been conducted to study the dead Li formation process and to develop measures for the prevention of dead Li. Both qualitative and quantitative approaches have been utilized to investigate Li plating/stripping behavior, such as operando nuclear magnetic resonance (NMR) spectroscopy, <sup>8, 9</sup> operando neutron depth profiling, <sup>10</sup> *in-situ* transmission electron microscopy (TEM), <sup>11, 12</sup> and *in-situ* optical microscopy <sup>13, 14</sup>. Strategies that have been proposed to minimize the amount of dead Li include the use of an artificial protective layer, <sup>15, 16</sup> reactivating dead Li by the use of additives in the electrolyte, <sup>17-19</sup> and creating a lithophilic surface

via surface chemistry tuning. <sup>20</sup> A simple strategy to minimize dead Li is to inhibit dendrite growth in the first place. The structural morphology of the dendrites, particularly the whisker type, makes them very prone to losing structural connection and forming dead Li during Li dissolution. Whisker dendrites can easily dissolve and detach from the anode at the base due to the narrower neck of the dendrite base. <sup>21</sup> On the other hand, chunky dendrites, having large diameters, are less prone to dead Li formation. <sup>22</sup> Once the dendrites form on the Li anode surface, they become more severe in the next cycles due to the formation of pits or caves, which increases the Li anode surface roughness and hence accelerates the dendrite formation. Consequently, the amount of dead Li also increases in the next cycles, leading to severe performance loss. Unlike bare Li, Li anode covered with a suitable protective layer performs smoothly even at higher cycles without forming dendrites and dead Li, increasing the life span of batteries. <sup>23</sup> The protective layer reduces the concentration polarization of Li<sup>+</sup> and electric field segregation on the Li surface by homogenizing the Li<sup>+</sup> flux, resulting in dendrite-free deposition. <sup>24</sup> Since the protective layer inhibits dendrite growth, the chances of dead Li formation are lower during the stripping process.

In parallel, theoretical studies such as phase-field modeling have proven to be very effective in simulating Li dendrite growth and dead Li formation in Li metal batteries. In 2003, Monroe and Newman <sup>25</sup> developed the first theoretical electrochemical model to simulate Li dendrite growth in a lithium-polymer cell. In 2004, Guyer *et al.* developed an equilibrium linear phase-field model to study electrochemistry and later advanced their model to explore electrodeposition kinetics in one dimension. <sup>26, 27</sup> Based on these earlier models, Liang *et al.* <sup>28</sup> developed a one-dimensional non-linear phase-field model to study electrode-electrolyte interface evolution. In recent years, the phase-field method has been further developed to study multiple factors affecting dendrite growth such as mechanical stress and strain, <sup>29, 30</sup> external pressure, <sup>31, 32</sup> grain boundaries and porosity of

solid electrolyte, <sup>33, 34</sup> thermal effects, <sup>35</sup> and the effect of a protective layer. <sup>36, 37</sup> Nonetheless, the phase-field method has been less developed and utilized to study dead Li formation. Recently, Zhang *et al.* developed a non-linear phase-field model to study dead Li formation in LMBs. <sup>38</sup> More recently, Gao *et al.* and Shen *et al.* studied the effect of external pressure on dendrite growth and dead Li formation using the phase-field method. <sup>32, 39</sup> However, these models are limited to investigating simple Li plating and stripping behaviors and lack a detailed and comprehensive study of the cycling process. In addition, the effect of a protective layer on Li plating/stripping cycles has been barely studied using phase-field methods.

In this work, we developed a phase-field model to study the dynamic morphological evolution of Li anode during plating/stripping processes. To be consistent with the real situations, we employed potentiostatic conditions for the charging process and galvanostatic conditions for the discharging process. First, we studied the cycling process in a bare Li anode and later introduced a protective layer on top of the Li anode. Temporal evolutions of Li<sup>+</sup> concentration and electric potential were studied. Effects of the geometry of dendrites on dead Li formation were also explored. In addition, the effects of a fractured protective layer on Li plating/stripping were investigated. Our simulation results thus provide fundamental insight into the plating and stripping behavior during the cycling process in LMBs.

#### 2. Methods

In this work, a half-cell model comprising a Li anode, a protective layer attached on top of the Li anode, and an electrolyte solution was used for the investigation. Order parameters  $\xi_1$  and  $\xi_2$  were introduced to describe Li anode ( $\xi_1 = 1$ ,  $\xi_2 = 0$ ), protective layer ( $\xi_1 = 0$ ,  $\xi_2 = 1$ ), and electrolyte ( $\xi_1 = 0$ ,  $\xi_2 = 0$ ), and their values continuously change from 0 to 1 across the interface. The components

of the electrolyte solutions are cations (Li<sup>+</sup>) and anions (A<sup>-</sup>), and only cations (Li<sup>+</sup>) are assumed to be mobile. It is assumed that the lithium metal surface has enough electrons (e<sup>-</sup>) to reduce all the incoming Li<sup>+</sup> into Li atom (Li<sup>+</sup> + e<sup>-</sup>  $\rightarrow$  Li) and deposit on the Li anode surface. Additionally, it is assumed that the protective layer is a good ionic (Li<sup>+</sup>) conductor but a bad conductor for electrons, i.e., its electrical conductivity is very low. Finally, the system is assumed to be isothermal, and all the simulations were performed at room temperature.

Based on our previous work, <sup>36</sup> the total free energy of the half-cell battery system is,

$$F = \int_{V} [f_{ch}(C_i, \xi_1, \xi_2) + f_{elec}(\phi, C_i) + f_{grad}(\nabla \xi_1, \nabla \xi_2)] dV$$
 (1)

where  $f_{grad}$ ,  $f_{ch}$  and  $f_{elec}$  are gradient energy density, Helmholtz free energy density, and electrostatic energy density, respectively. The Helmholtz free energy is the combination of local free energy density ( $f_0$ ) and ion mixing energy ( $f_{ion}$ ). The local free energy density takes the form  $f_0 = W_1 \xi_1^2 (1 - \xi_1)^2 + W_2 \xi_2^2 (1 - \xi_2)^2 + \frac{3}{2} \xi_1^2 \xi_2^2$ , where  $W_1 = 0.25$  and  $W_2 = 0.15$  are the energy barrier height of the double-well function for the Li anode and protective layer, respectively, and  $\frac{3}{2} \xi_1^2 \xi_2^2$  is a cross-term that yields three minimum values for three equilibrium regions i.e., for Li anode, protective layer, and electrolyte. The gradient energy density can be written as  $f_{grad} = \frac{\kappa_1}{2} (\nabla \xi_1)^2 + \frac{\kappa_2}{2} (\nabla \xi_2)^2$ , where where  $\kappa_1$  and  $\kappa_2$  are the gradient energy coefficients of lithium metal and protective layer, respectively. We added an anisotropic gradient energy coefficient takes the form  $\kappa_1 = \kappa_0 [1 + \delta \cos(\omega \theta)]$ , where  $\kappa_0$ ,  $\delta$ ,  $\omega$ , and  $\theta$  denote the surface energy coefficient, strength of anisotropy, mode of anisotropy, and the angle between the reference axis and vector normal to Li interface, respectively. The complete descriptions of the above energy densities are provided in the literature.  $^{40,41}$ 

The temporal evolution of order parameter  $\xi_1$  during charging is governed by the equation,

$$\frac{\partial \xi_1}{\partial t} = -L_{\xi_1} \left\{ \frac{\partial f_{ch}}{\partial \xi_1} - \kappa_1 \left( \nabla^2 \xi_1 \right) \right\} - L_{\eta} h'(\xi_1) \left\{ exp \left[ \frac{\alpha z F \eta}{RT} \right] - C_{Li^+}^* exp \left[ \frac{-\beta z F \eta - z F \eta_m}{RT} \right] \right\}$$
 (2)

where t is the simulation time,  $L_{\xi_1}$  is interfacial mobility for Li metal,  $L_{\eta}$  is the reaction constant, z is the valence of Li<sup>+</sup>, and  $\eta$  is the overpotential for the reaction.  $h(\xi_1) = \xi_1^3 (10 - 15\xi_1 + 6\xi_1^2)$  is an interpolation function and  $h'(\xi_1) = \partial h(\xi_1)/\partial \xi_1$  confines the charge transfer reaction (Li<sup>+</sup> + e<sup>-</sup> = Li) to be at the Li/electrolyte interface.  $\alpha = \beta = 0.5$  are the symmetric factors ( $\alpha + \beta = 1$ ), R is the universal gas constant, and R is a temperature in Kelvin.  $R_m = \frac{\sigma V_m}{F}$  is an additional term induced by the mechanical stress ( $\sigma$ ) which modifies the overpotential, where  $R_m = 1.3 \times 10^{-5}$   $R_m^3/mol$  is the molar volume of Li, and R is Faraday's constant.

During the discharging process, the temporal evolution of order parameter  $\xi_1$  takes the form,

$$\frac{\partial \xi_1}{\partial t} = -f_d L_{\xi_1} \left\{ \frac{\partial f_{ch}}{\partial \xi_1} - \kappa_1 \left( \nabla^2 \xi_1 \right) \right\} - f_d L_{\eta} h'(\xi_1) \left\{ exp \left[ \frac{\alpha z F \eta - z F \eta_m}{RT} \right] - C_{Li^+}^* \right. \\ \left. exp \left[ \frac{-\beta z F \eta}{RT} \right] \right\}$$
 (3)

where  $f_d = step(\frac{\phi}{\phi_c - 0.01})$  is a step function whose value steps from 0 to 1 at  $\frac{\phi}{\phi_c - 0.01} > 1$ , i.e., when  $\frac{\phi}{\phi_c - 0.01} > 1$ ,  $f_d = 1$  and when  $\frac{\phi}{\phi_c - 0.01} < 1$ ,  $f_d = 0$ .  $f_d = 1$  represents active lithium, whereas  $f_d = 0$  represents dead lithium.  $\phi$  is electric potential and  $\phi_c$  is a reference electric potential whose value is equivalent to the potential of the active Li anode.

To apply the effect of mechanical stress on the Li cycling process, we solve the mechanical equilibrium equation to obtain the local elastic stress distribution. The mechanical equilibrium equation is expressed as,

$$\nabla \cdot \boldsymbol{\sigma} = 0 \tag{4}$$

where  $\sigma = C^{ST} \varepsilon^{el}$  and  $\varepsilon^{el} = \varepsilon^T - \varepsilon^0$ .  $\varepsilon^{el}$ ,  $\varepsilon^0$ , and  $\varepsilon^T$  are the elastic strain, inelastic strain, and total strain, respectively.  $C^{ST}$  is the elastic stiffness tensor whose value depends on elastic modulus and Poisson's ratio. The inelastic strain is generated due to the volume expansion of the Li anode during deposition and can be expressed by  $\varepsilon^0 = V_g \xi_1$ .  $V_g$  is a diagonal matrix composed of Vegard's strains coefficient, also known as the eigenvalue of strain tensor, and its value is obtained from the literature. <sup>29</sup> We assumed plane strain conditions for our model.

The temporal evolution of the protective layer  $(\xi_2)$  is expressed by the following equation,

$$\frac{\partial \xi_2}{\partial t} = -L_{\xi_2} \left\{ \frac{\partial f_{ch}}{\partial \xi_2} - \kappa_2 (\nabla^2 \xi_2) \right\} - D_f \qquad (5)$$

where  $L_{\xi_2}$  and  $\kappa_2$  are interfacial mobility and gradient energy coefficient for the protective layer, respectively.  $D_f$  is a driving force that is responsible for the motion of the protective layer during Li surface movement. Based on our earlier work,  $^{36}$  we define  $D_f$  as

$$D_f = \left[ max\{ -h'(\xi_1)h'(\xi_2)\Delta G\} \frac{\partial \xi_2}{\partial x} + Cd_m \right] b \qquad (6)$$

where  $\Delta G$  is the Butler-Volmer expression defined in Eq. (2), and b is a driving force constant.  $d_m = \frac{\sigma l^3}{48E_p I_p}$  is an additional driving force term that captures the deflection of the protective layer caused by mechanical stress during Li deposition, and C is a calibration factor. We used the maximum deflection of a beam theory  $\delta_{max} = \frac{P l^3}{48E_p I_p}$  to determine  $d_m$  caused by the stress, where P is the force; l,  $E_p$ , and  $I_p$  are the length, modulus of elasticity, and moment of inertia of the protective layer, respectively. <sup>42</sup> We replace force (P) with stress ( $\sigma$ ) to make sure that the unit of  $d_m$  becomes  $m^{-1}$ , which is compatible with  $D_f$  in Eq. (6). Furthermore, a calibration factor (C) is also included in Eq. (6) to simulate accurate deflection of a protective layer. It is seen that  $d_m$  is

inversely proportional to  $E_p$ , indicating that a higher modulus of elasticity of the protective layer can better suppress the dendrite growth. An experimental study suggests that protective layer with modulus of elasticity value of 6.85 GPa is sufficient to suppress the Li dendrites. <sup>43</sup>

The temporal evolution of Li<sup>+</sup> concentration is governed by the Nernst-Plank equation,

$$\frac{\partial C_{Li^+}^*}{\partial t} = \nabla \cdot \left[ D^{eff} \nabla C_{Li^+}^* + \mu_{Li} C_{Li^+}^* z F \nabla \phi \right] - K \frac{\partial \xi_1}{\partial t} \quad (7)$$

where K is a constant that defines the annihilation/accumulation rate of the Li<sup>+</sup> at the Li interface,  $\phi$  is electric potential,  $\mu_{Li}$  is the mobility of Li<sup>+</sup>, and z is the valence number.  $D^{eff} = D_e h(\xi_1) + D_s(1 - h(\xi_1) - h(\xi_2)) + D_p h(\xi_2)$  is the effective diffusivity of the Li<sup>+</sup> and  $h(\xi_2) = \xi_2^3 (10 - 15 \xi_2 + 6\xi_2^2)$  is an interpolation function defined by  $\xi_2$ , where  $D_e$ ,  $D_s$ , and  $D_p$  are the diffusivity of Li<sup>+</sup> in the Li metal, electrolyte, and protective layer, respectively.

Assuming the system to be charge neutral, the electric potential distribution is calculated by solving the current continuity equation,

$$\nabla \cdot \left(\sigma^{eff} \nabla \phi\right) = R_e \frac{\partial \xi_1}{\partial t} \quad (8)$$

where  $\sigma^{eff} = \sigma_e h(\xi_1) + \sigma_s (1 - h(\xi_1) - h(\xi_2)) + \sigma_p h(\xi_2)$  is the effective electric conductivity of the system;  $\sigma_e$ ,  $\sigma_s$  and  $\sigma_p$  are the electrical conductivity of Li anode, electrolyte solution, and protective layer, respectively. Since the protective layer is assumed to be electrically insulative, we approximate  $\sigma_p = \sigma_s$  for our simulations.  $R_e$  is a current constant.

It is more realistic to apply galvanostatic conditions for the discharging process, i.e., the current density remains constant while the electric potential may change. The discharging current density can be approximated using the Tafel equation, <sup>44</sup>

$$\hat{I} \approx I_0 exp \left\{ \frac{\alpha z F \eta}{RT} \right\}$$
 (9)

where  $I_0$  is an exchange current density. The total current depends on the Li metal interfacial area where an electrochemical reaction (exchange of electrons) occurs. Therefore, the current density can be assumed to be proportional to the surface area of the Li interface by modifying Eq. (9),

$$I \approx I_0 exp \left\{ \frac{\alpha z F \eta}{RT} \right\} \frac{S}{S_0}$$
 (10)

where *S* is the interfacial area of Li metal, and  $S_0$  is the initial interfacial area of Li metal at t = 0 s. We define the Li interfacial region as  $0.05 < \xi_1 < 0.95$ .

The overpotential can be obtained by solving Eq. (10) as follows,

$$\eta \approx \frac{RT}{z\alpha F} ln \left\{ \frac{I}{I_0} \frac{S_0}{S} \right\}$$
(11)

Our phase-field model was developed based on the COMSOL Multiphysics platform and all the equations were solved using finite element methods. The model geometry consists of a two-dimensional square-shaped domain with the size 500  $\mu$ m × 500  $\mu$ m. The real parameters were converted into normalized parameters using characteristics length ( $l_0$ ), characteristics time ( $\Delta t_0$ ), and characteristics energy ( $E_0$ ). The detailed formulas for parameter conversion, real values, and their normalized values are shown in Table 1. Zero flux boundary conditions were applied for parameters  $\xi_1$  and  $\xi_2$ , while Dirichlet boundary conditions were applied for electric potential ( $\phi$ ) and Li<sup>+</sup> concentration ( $C_{Li^+}$ ). The Li<sup>+</sup> concentration ( $C_{Li^+}$ ) is normalized by dividing with the bulk concentration of Li<sup>+</sup> ions, i.e,  $C_{Li^+}^* = C_{Li^+}/C_0$ , where  $C_0 = 1$  mol/L. For the charging process, electrical potential  $\phi$  is set as a fixed value at both left boundary ( $\phi = -0.35$  V) and right boundary ( $\phi = 0$  V), whereas the value of  $C_{Li^+}^*$  is set to be 1 at the right boundary. Similarly, for the discharging process, the value of  $\phi$  is set to be 0 V at the right boundary, while it is set as a variable

at the left boundary. A schematic illustration showing boundary conditions can be found in the supporting information (**Figure S1**). The Li<sup>+</sup> concentration in the electrolyte solution is set to be 1 mol/L.

**Table 1**. List of parameters and their normalized values.

Parameters	Symbol	Real Value	Normalization	Normalized value	References
Interfacial mobility for Li	$L_{\xi 1}$	$2.5 \times 10^{-6} m^3$ /(J × s)	$\hat{L}_{\xi 1} = L_{\xi 1} \times (E_0 \times \Delta t_0)$	3750	[ <sup>41</sup> ]
Reaction constant	$L_{\eta}$	0.001/s	$\hat{L}_{\eta} = L_{\eta} \times \Delta t_{0}$	1	$[^{36}]$
Interfacial mobility for protective layer	$L_{\xi 2}$	$2.65 \times 10^{-7} m^3$ /(J × s)	$\hat{L}_{\xi 2} = L_{\xi 2} \times (E_0 \times \Delta t_0)$	600	[36]
Barrier Height	$W_1$	$3.75\times 10^5~J/m^3$	$\hat{W}_1 = W_1 / E_0$	0.25	[ <sup>41</sup> ]
Li <sup>+</sup> diffusivity in electrolyte	$D_s$	$2.5 \times 10^{-12}  m^2$ /s	$\hat{D}_s = D_s / (l_0^2 / \Delta t_0)$	1	[40]
Li <sup>+</sup> diffusivity in electrode	$D_e$	$2.5 \times 10^{-15}  m^2$ /s	$\hat{D}_e = D_e / (l_0^2 / \Delta t_0)$	0.001	[40]
Electrical conductivity of electrolyte	$\sigma_{\scriptscriptstyle S}$	0.1 <i>S/m</i>	$\hat{\sigma}_s = $ $\sigma_s / ((l_0^2 / \Delta t_0) \times (c_0 F^2 / RT))$	10	[ <sup>29</sup> ]
Electrical conductivity of electrode	$\sigma_e$	$1 \times 10^6  S/m$	$\hat{\sigma}_e = \frac{\hat{\sigma}_e - \hat{\sigma}_e}{\sigma_e / ((l_0^2 / \Delta t_0) \times (c_0 F^2 / RT))}$	$1 \times 10^8$	[ <sup>29</sup> ]
Gradient energy coefficients	$k_1,k_2$	$5\times 10^{-5}J/m$	$\hat{k} = k/(E_0 \times l_0^2)$	0.01	[ <sup>41</sup> ]
Charge transfer coefficient	$\beta$ , $\alpha$	0.5	-	-	
Driving force constant	b	$6\times 10^{-10}m/s$	$\hat{b} = b \times (\Delta t_0 / l_0)$	0.01	Calculated
Modulus of elasticity for Li	$E_e$	4.9 <i>GPa</i>	$\hat{E}_e = E_e/E_0$	3260	[29]
Modulus of elasticity for protective layer	$E_p$	10 <i>GPa</i>	$\hat{E}_p = E_p / E_0$	6660	Estimated
Moment of inertia for protective layer	$I_p$	$5.21 \times 10^{-18}  m^4$	$\hat{I}_p = I_p / l_0^4$	0.6	Calculated
Vegard's strain coefficients	$V_{g11}$	$-0.86 \times 10^{-3}$		$-0.86 \times 10^{-3}$	[29]
	$V_{g22}$	$-0.77 \times 10^{-3}$		$-0.77 \times 10^{-3}$	[29]
	$V_{g33}$	$-0.52 \times 10^{-3}$		$-0.52 \times 10^{-3}$	[29]

# 3. Results and Discussions

## 3.1 Charging/discharging behavior in a bare Li anode.

First, we simulated the charging and discharging behaviors in a bare Li anode/electrolyte halfcell model. We assume that the initial morphology of the Li anode consists of a flat surface with a semi-circle protrusion at the surface center, which mimics the surface roughness (Figure 1a). During Li plating, the dendritic volume and morphologies are determined by both nucleation and growth. When the applied overpotential is greater than the critical overpotential for nucleation, Li embryos with a critical kinetic radius nucleate and grow. The nuclei which are kinetically and thermodynamically stable start to grow at constant terminal velocity. After the formation of stable lithium nuclei, the shape and microstructural development of the deposits are primarily influenced by localized electric fields and morphological instabilities. 45 During the first charging, the protrusion grows into a long filament-shaped dendrite while the flat surface becomes thicker due to electrodeposition ( $Li^+ + e^- \rightarrow Li$ ), as shown in **Figure 1c**. Nucleation and growth of smaller dendrites can also be seen at the top and bottom regions of the Li anode surface, which is mainly caused by small surface roughness. After nucleation, the dendrite growth was accelerated by the non-uniform distribution of electric field and Li<sup>+</sup> flux over the surface of the Li anode, i.e., these values become higher at the tip of dendrites (Figure S2). The evolutions of Li<sup>+</sup> concentration and electrical potential during the charging process are shown in Figure 1d-f and Figure 1g-i, respectively.

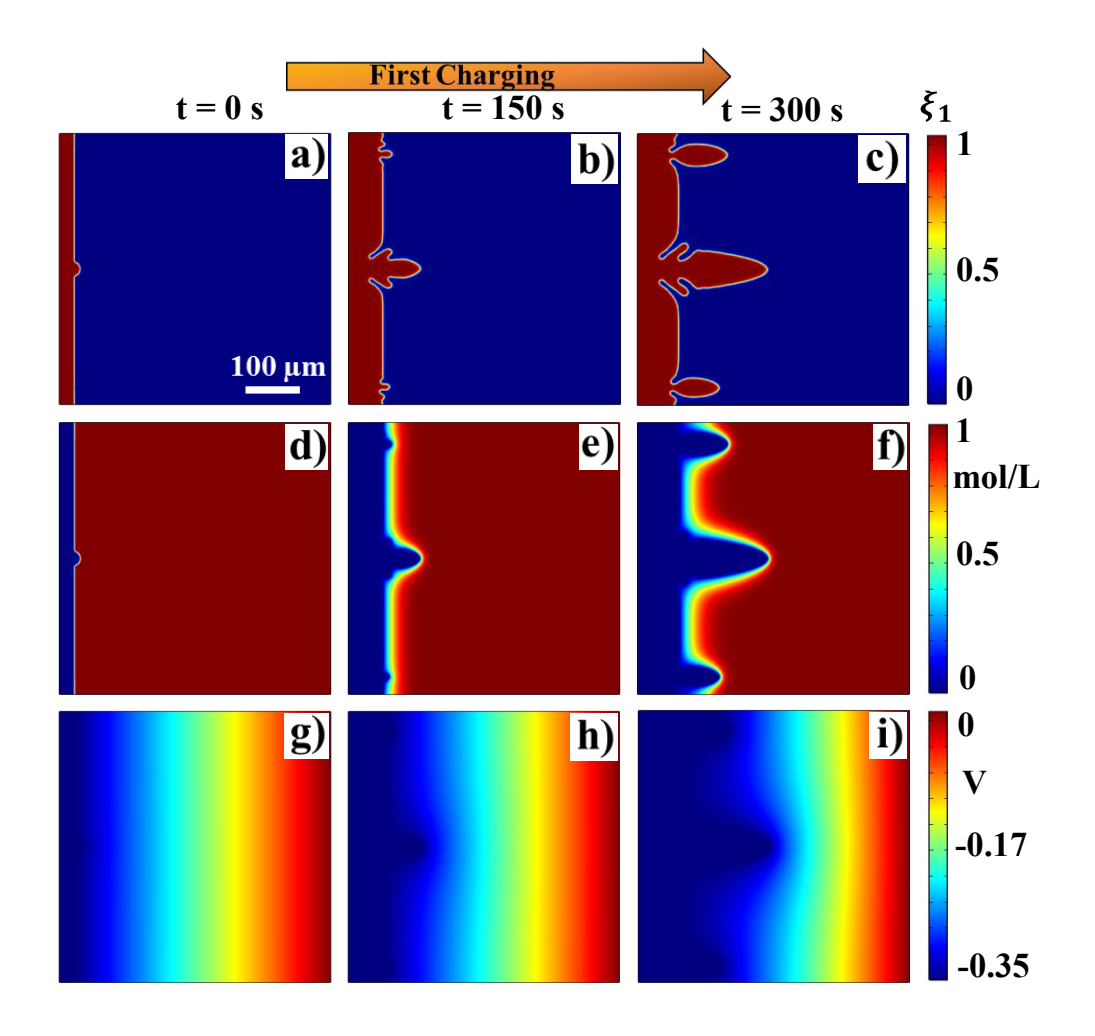


**Figure 1**. Simulation results showing the first charging process in a bare Li anode. **(a-c)** morphologies of Li anode at 0-300 s. The initial protrude grows into a large filament-like dendritic structure. **(d-f)** Li<sup>+</sup> concentration. **(g-i)** Electrical potential.

During the first discharging process, the final morphology of Li (t = 300s) from the first charging (**Figure 1c**) is taken as the initial condition, as shown in **Figure 2a**. The cell was discharged at a constant current density of 2 mA/cm<sup>2</sup>. It is seen that during the Li stripping process, the volume of the Li anode gradually decreases over time due to Li dissolution caused by the reverse reaction (Li  $\rightarrow$  Li<sup>+</sup> + e<sup>-</sup>), and dendrites are detached from the bulk electrode and turned into inactive lithium, also known as "dead Li" (**Figure 2a-c**). Once formed, these dead

Li can no longer participate in further electrochemical reactions (Li<sup>+</sup> + e<sup>-</sup> = Li), as a solidelectrolyte interface (SEI) layer will form around the dead Li, blocking electrons in Li anode from conducting to these dead Li. <sup>17</sup> The first dead lithium appeared after 80 seconds and its amount increased over time until all dendrites were completely disconnected from the anode, as shown in **Figure 2j**. Furthermore, the Li<sup>+</sup> concentration becomes very high at the active Li metal surface due to Li atoms rapidly converting into Li<sup>+</sup> ions. On the other hand, Li<sup>+</sup> concentration remains much lower near the surface of dead Li, as the electrochemical reaction (Li  $\rightarrow$  Li<sup>+</sup> + e<sup>-</sup>) cannot occur. These are clearly shown in **Figure 2e**, **f**. Finally, the surface area of the Li anode gradually decreased throughout the stripping process, which eventually reduced the current. Therefore, the electrical potential ( $\phi$ ) increased with time (**Figure 2k**) to maintain the constant current density. These results agree well with the previous study. <sup>38</sup> It is also seen that at the end of the stripping process, the surface of the Li anode becomes highly rough (**Figure 2c**), which is expected to influence the subsequent cycling.

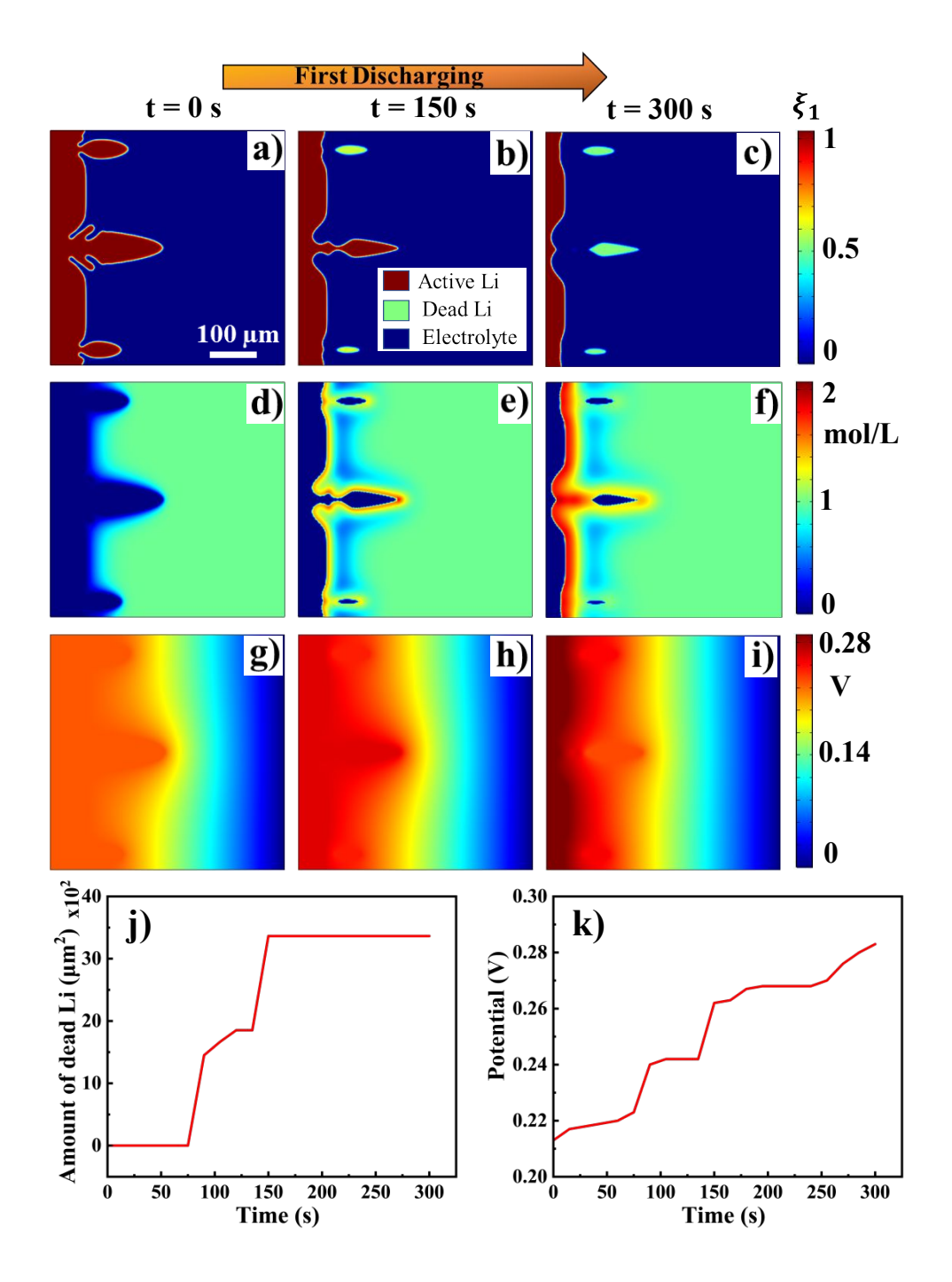


**Figure 2**. Simulation results showing the first discharging process in a bare Li anode. (a-c) morphologies of Li anode at 0-300 s. During discharging, the dendrites turn into dead lithium. (d-f) evolution of Li<sup>+</sup> concentration. (g-i) evolution of electrical potential. (j) amount of dead lithium versus time. (k) electric potential of Li anode versus time.

To further explore the cycling process, we simulated the second charging and discharging cycle. For the second charging, we choose the final shape of the Li anode from the first discharging process (Figure 2c) as the initial condition. The initial Li anode surface consists of pits or caves (Figure 3a) that were formed during the first stripping process, which increased the surface roughness. Soon after the second charging process starts, Li atoms nucleate on multiple sites all over the Li anode surface (Figure 3b) and later grow into large dendrites (Figure 3d). The growth of these multiple dendrites was caused by uneven electrode surface roughness which increases the number of active nucleation sites, also known as "hot spots", on the surface and Li atoms preferentially nucleate on these sites because of reduced deposition interface energy. 46, 47 Compared with the first charging process (Figure 1c), the Li surface after the second charging resulted in more dendrites (Figure 3d). Similar formation of caves or pits during the discharging process and the subsequent increases in nucleation sites and the number of dendrites in the next cycle were also observed in previous experiments. <sup>6, 13, 48</sup> Therefore, our simulation results agree well with experimental results. Additionally, during the second discharging, the total quantity of dead lithium increased (Figure 3h) as compared to dead lithium in the first discharging process (Figure 2c). Also, the surface roughness of the Li anode increased after the second discharge (**Figure 3h**). Therefore, the Li dendrite growth and the subsequent dead Li formation is a selfaccelerating process. <sup>49</sup> These dead Li will further accumulate and form a compact layer on the surface of the Li anode, hindering the mass transport of Li<sup>+</sup> ions. <sup>6, 48</sup> The loss of active Li anode materials due to dead Li eventually causes capacity loss and failure of the battery. The Li<sup>+</sup> concentration and electric potential corresponding to each state in Figure 3 can be found in Figure **S3**.

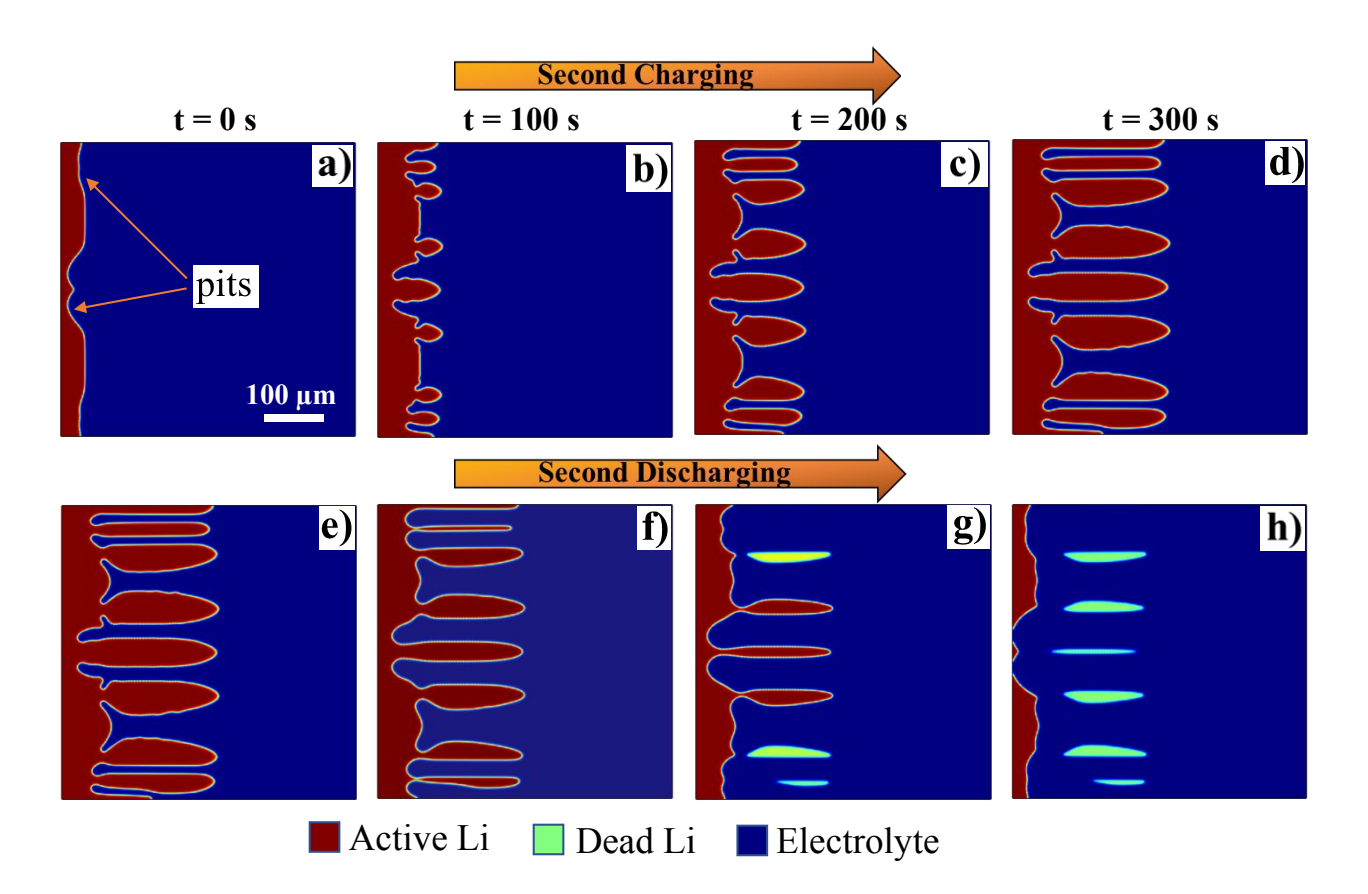


**Figure 3**. Simulation results showing the morphological evolution of Li anode during **(a-d)** second charging, and **(e-h)** second discharging.

#### 3.2 Effect of the geometry of dendrites on dead lithium formation.

In addition to the regular charging and discharging cycles, we further study the effect of the geometry of the dendrites on dead lithium formation. For this study, we assumed four filament-shaped dendrites of similar size and shape, but with different neck/root widths. The initial neck/root width of the dendrites is set as 8  $\mu$ m, 11  $\mu$ m, 13  $\mu$ m, and 16  $\mu$ m, as shown in **Figure 4a**. During the stripping process, it is seen that the dendrites having the smallest neck width (8  $\mu$ m) detach from the electrode first, while the dendrites having the largest neck width (16  $\mu$ m) detach last (**Figure 4b-d, g**). It is also found that the amount of dead Li formed from a specific Li dendrite decreases with increasing neck width (**Figure 4e,f**). This is because as soon as the dendrites are detached from the active electrode, they become inactive and do not participate in the

electrochemical reactions. Since dendrites with thicker necks remain connected to the active Li anode and undergo electrochemical reactions for a longer time, more Li atoms are oxidized into Li<sup>+</sup> in the electrolyte, and the final size of the dead Li becomes smaller. Several theoretical and experimental studies on the Li dissolution phenomenon have been performed. For example, Yamaki et al. <sup>50</sup> developed a theoretical model to study the Li dissolution process for whiskershaped dendrites and found that at the beginning the dissolution occurred at the tips and kinks of the Li whisker and later it dissolved at the base. Furthermore, dendrites with small diameters easily detached from the electrode and produced a large amount of dead Li. Recently, Lee et al. 49 used molecular dynamics simulation to study the dissolution of filament-shaped Li dendrites during the discharging process. They found that the dendrites dissolution process happened at certain localized areas, especially at the bottom part, resulting in the formation of dead Li. Similarly, through experimental studies, Fang et al. 22 compared the inactive Li formation mechanism between dendrites of "whisker" morphology (small diameter) and of "chunky" morphology (wide diameter). Their results show that whisker-type dendrites easily lost structural connection and formed a large amount of dead Li, whereas chunky dendrites maintained good structural connection and formed a small amount of dead Li. Therefore, our phase-field results agree well with previous theoretical and experimental results from the literature.

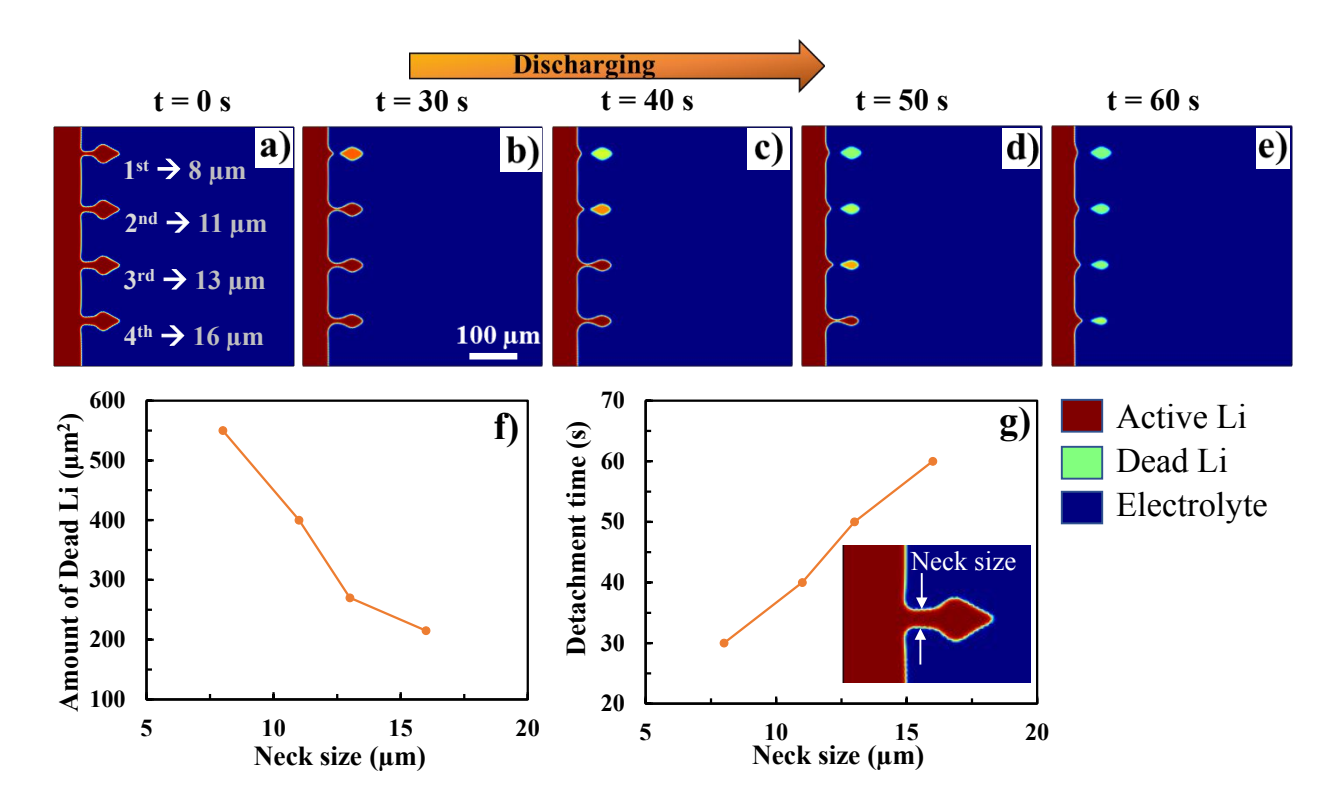


**Figure 4**. Simulation results showing the effect of the geometry of dendrites on dead lithium formation during stripping. (a-e) morphological evolution of dendrites during stripping (0 - 60 s). (f) Neck size versus the amount of dead lithium. (g) Neck size versus detachment time of dendrites from the bulk electrode.

#### 3.3 Charging/discharging behavior of Li anode with the protective layer.

Next, we include a protective layer on top of the Li anode to study its effect on the cycling process. The thickness of the protective layer is set as 50  $\mu$ m. For convenience, it is assumed that the diffusivity of Li<sup>+</sup> in the protective layer ( $D_p$ ) is equal to that in the electrolyte ( $D_s$ ), i.e.,  $D_p = D_s$ . Equations (2), (4), (5), (7), and (8) were coupled and solved to obtain the results. The initial morphology of the Li anode is the same as in section 3.1, however, it is completely covered by a protective layer that moves along with the Li surface displacement. During the first charging, the Li metal flat surface becomes thicker due to electrodeposition, while the size of the protrusion almost remains the same (**Figure 5a-c**). The protective layer physically prevents the protrusion

from growing into dendrites, enabling the smooth deposition of Li metal. Additionally, the protective layer homogenizes the Li<sup>+</sup> ion flux by reducing large concentration and potential gradient at the Li surface (**Figure S5**), resulting in a dendrite-free Li deposition. <sup>36, 51</sup> The Li<sup>+</sup> concentration and electric potential can be found in supporting information (**Figure S4**).

During the first discharging, the thickness of the Li anode decreased over time as more and more Li atoms were dissolved to form Li<sup>+</sup> ions. Unlike the bare Li anode, no dead Li was formed when the Li anode was covered with the protective layer (**Figure 5d-f**). The dead Li is usually formed by the structural disconnection of dendrites from the bulk electrode. Since the dendrite growth was inhibited by a protective layer during plating, no dead Li was formed during stripping. Furthermore, during the second charging, Li metal again grew smoothly without forming any dendrites (**Figure 5g-i**), similar to the first charging process. Consequently, in the second discharging process, the Li anode dissolved smoothly without the formation of dead lithium (**Figure 5j-l**). Hence, our simulation results indicate that the protective layer not only inhibits dendrite growth but also prevents the formation of dead Li. Experimental studies have verified that a suitable protective layer can prevent dendrite growth and dead Li formation in LIBs. <sup>52-54</sup>

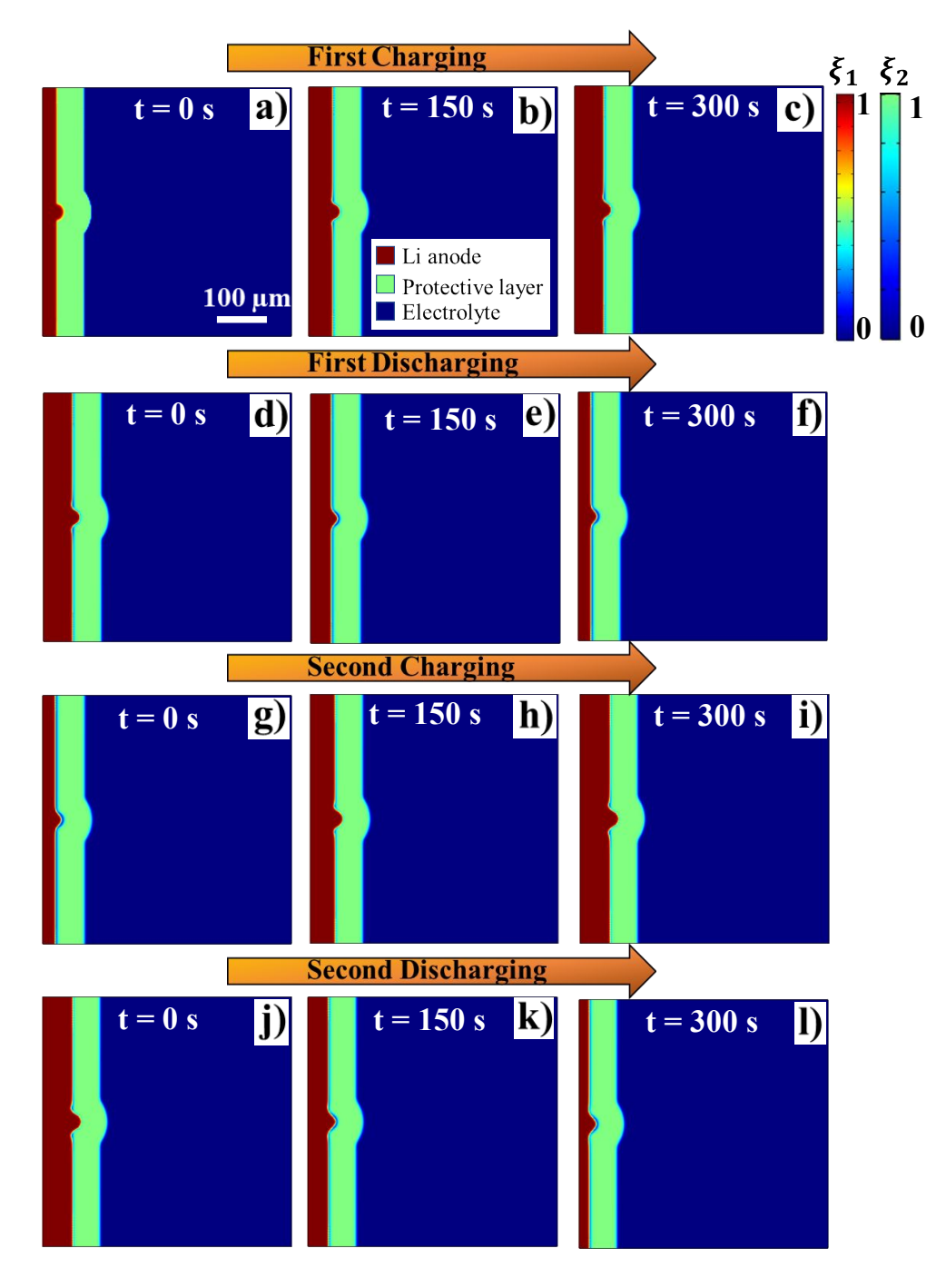


**Figure 5**. Simulation results showing the charging/discharging behavior of Li metal in the presence of a protective layer. Morphological evolution of Li metal and protective layer during; **(a-c)** first charging; **(d-f)** first discharging; **(g-i)** second charging; **(j-l)** second discharging. The scale bar in **(a)** applies to all the figures.

### 3.4 Effect of a fractured protective layer on the cycling process.

Finally, we study the effect of a fractured protective layer on Li plating/stripping behavior. During Li deposition, high stress may be induced due to volume expansion of Li atoms, and the local high stress could damage the protective layer, i.e., cracks may form. <sup>16</sup> If the local stress at the tip of the cracks exceeds the critical stress value, the cracks will propagate over time, resulting in the fracture of the protective layer. <sup>55</sup> Once the protective layer is fractured, fresh Li is exposed to the electrolyte, leading to irreversible capacity loss caused by the consumption of Li atoms and electrolytes. <sup>56</sup> In addition, Li metals will rapidly grow into the crack hole due to a large electric field and enhanced Li<sup>+</sup> flux at the tip of the protrusion, which eventually turns into dendrites. <sup>57, 58</sup> To study these behaviors, we employed a protective layer with a pre-existing crack at the center, as shown in **Figure. 6a**. The size of the crack hole is approximately 12 μm. During charging, Li metal rapidly grows into the crack in the form of protrusion and soon penetrates the protective layer. After penetration, it continues to grow into a large dendritic structure (Figure 6d). To understand the mechanism of this phenomenon, we plot the electric field and Li<sup>+</sup> flux (calculated as the product of diffusivity and concentration gradient) at different time frames. It is seen that the electric field is concentrated at the tip of the dendrite (Figure 6f-h). Similarly, the Li<sup>+</sup> flux is initially higher at the tip of the protrusion (Figure 6j), and after penetration the flux is still higher around the surface of the dendrite, whereas it is low at the flat surface (Figure 61). The higher flux and large electric field caused the protrusion to grow rapidly and penetrate the protective layer. It is seen that the large dendrite thus formed is structurally connected to Li electrode by a narrow neck/base passing through the crack hole. Consequently, during discharging, the dendrite quickly dissolved at the base and easily disconnected from the metallic electrode, resulting in large dead Li on the other side of the protective layer (**Figure 6p**). Our simulation indicates that the existence

of a crack inside the protective layer can even accelerate the dead Li formation. Similar phenomena of crack formation and penetration of the protective layer by dendrite during Li plating and formation of dead Li during stripping were also observed in experimental studies. <sup>16, 55</sup>

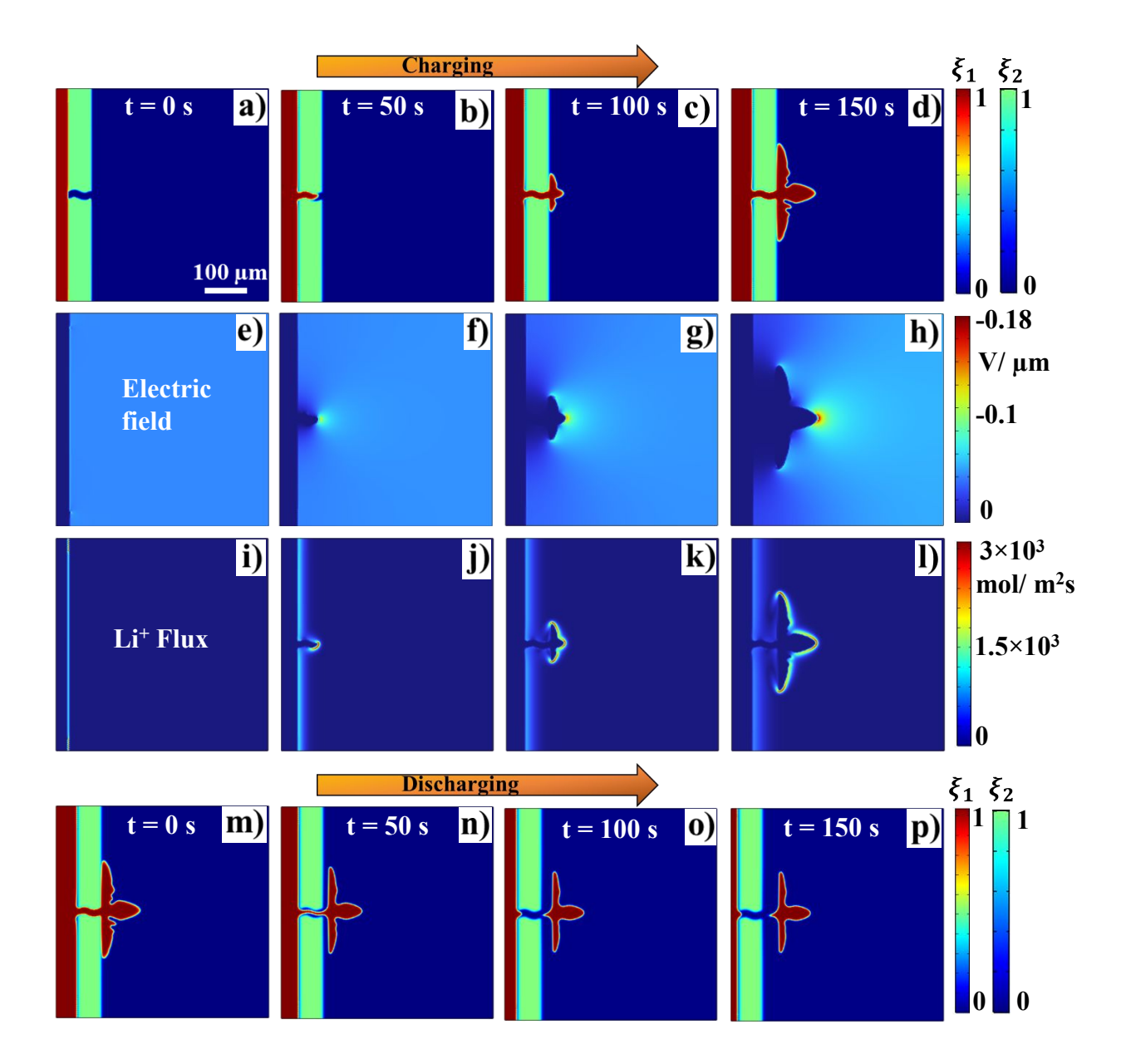


**Figure 6**. Charging/discharging behavior of Li metal with a fractured protective layer. **(a-d)** Evolution of Li metal (red region) and a protective layer (green region) during charging. **(e-h)** Electric field during charging. **(i-l)** Li<sup>+</sup> flux during charging. **(m-p)** Morphologies of Li metal and protective layer during discharging. The scale bar in **(a)** applies to all figures.

#### 4. Conclusion

In summary, we developed a phase-field model to successfully simulate the charging and discharging process in a bare Li anode and Li anode with a protective layer. In bare Li, the initial protrusion grows into filament-like dendrite during the first charging, and a small amount of dead lithium is produced during the first discharging. However, during the second charging, the number of dendrites increases due to the increase in surface roughness of the Li anode, which creates additional nucleation sites for dendrites to nucleate and grow into larger dendrites. Consequently, the amount of dead lithium also increases during the second discharge. Furthermore, it is found that dendrites with narrower necks/roots can easily detach from an anode and produce more dead lithium compared to dendrites having thicker necks/roots. In contrast, the charging and discharging cycles are much smoother with the protective layer. The protective layer prevents the dendrite nucleation and growth. As a result, no dead lithium is formed. Additionally, in the case of a fractured protective layer, Li deposition occurs rapidly inside the crack due to an enhanced electric field and Li<sup>+</sup> flux at the tip of protrusion and forms a larger dendrite. The dendrite breaks at the base and turns into dead Li after stripping, indicating that a crack that penetrates through the protective layer can accelerate the dead Li formation process. All our simulation results agree well with previous experimental reports. Our work thus contributes to a deeper understanding of the Li cycling process and can guide the design of an effective Li metal surface for highly efficient and long-lifespan LMBs.

#### ASSOCIATED CONTENT

# **Supporting Information**

Schematic illustration of boundary conditions; simulation results for Li<sup>+</sup> flux and electric field for bare Li anode and Li anode with a protective layer; plot of Li<sup>+</sup> concentration and electric potential for second charging and discharging.

#### **DECLARATION OF INTEREST**

The authors declare no competing financial interest.

#### **AUTHOR INFORMATION**

#### **Corresponding Author**

**Ye Cao** – Department of Materials Science and Engineering, University of Texas at Arlington, Texas 76019, United States.

Email: ye.cao@uta.edu

#### **Authors**

**Bharat Raj Pant** – Department of Materials Science and Engineering, University of Texas at Arlington, Texas 76019, United States

**Yao Ren** – Department of Materials Science and Engineering, University of Texas at Arlington, Texas 76019, United States

#### **ACKNOWLEDGEMENTS**

This work is supported by the US National Science Foundation (NSF) under awards No. 2038083 and No. 2425164.

#### 5. Reference

- (1) Zubi, G.; Dufo-López, R.; Carvalho, M.; Pasaoglu, G. The lithium-ion battery: State of the art and future perspectives. *Renewable and Sustainable Energy Reviews* **2018**, *89*, 292-308. DOI: https://doi.org/10.1016/j.rser.2018.03.002.
- (2) Liu, B.; Zhang, J.-G.; Xu, W. Advancing Lithium Metal Batteries. *Joule* **2018**, *2* (5), 833-845. DOI: <a href="https://doi.org/10.1016/j.joule.2018.03.008">https://doi.org/10.1016/j.joule.2018.03.008</a>.
- (3) Kim, S.; Park, G.; Lee, S. J.; Seo, S.; Ryu, K.; Kim, C. H.; Choi, J. W. Lithium-Metal Batteries: From Fundamental Research to Industrialization. *Advanced Materials* **2023**, *35* (43), 2206625. DOI: https://doi.org/10.1002/adma.202206625.
- (4) Cheng, X.-B.; Zhang, R.; Zhao, C.-Z.; Zhang, Q. Toward Safe Lithium Metal Anode in Rechargeable Batteries: A Review. *Chemical Reviews* **2017**, *117* (15), 10403-10473. DOI: https://doi.org/10.1021/acs.chemrev.7b00115.
- (5) Jiang, F.-N.; Yang, S.-J.; Liu, H.; Cheng, X.-B.; Liu, L.; Xiang, R.; Zhang, Q.; Kaskel, S.; Huang, J.-Q. Mechanism understanding for stripping electrochemistry of Li metal anode. *SusMat* **2021**, *1* (4), 506-536. DOI: <a href="https://doi.org/10.1002/sus2.37">https://doi.org/10.1002/sus2.37</a>.
- (6) Chen, K.-H.; Wood, K. N.; Kazyak, E.; LePage, W. S.; Davis, A. L.; Sanchez, A. J.; Dasgupta, N. P. Dead lithium: mass transport effects on voltage, capacity, and failure of lithium metal anodes. *Journal of Materials Chemistry A* **2017**, *5* (23), 11671-11681. DOI: https://doi.org/10.1039/C7TA00371D.
- (7) Lin, D.; Liu, Y.; Cui, Y. Reviving the lithium metal anode for high-energy batteries. *Nature Nanotechnology* **2017**, *12* (3), 194-206. DOI: https://doi.org/10.1038/nnano.2017.16.
- (8) Xiang, Y.; Tao, M.; Zhong, G.; Liang, Z.; Zheng, G.; Huang, X.; Liu, X.; Jin, Y.; Xu, N.; Armand, M.; Zhang, J.-G.; Xu, K.; Fu, R.; Yang, Y. Quantitatively analyzing the failure processes of rechargeable Li metal batteries. *Science Advances* **2021**, *7* (46), eabj3423. DOI: https://doi.org/10.1126/sciadv.abj3423.
- (9) Hsieh, Y.-C.; Leißing, M.; Nowak, S.; Hwang, B.-J.; Winter, M.; Brunklaus, G. Quantification of Dead Lithium via In Situ Nuclear Magnetic Resonance Spectroscopy. *Cell Reports Physical Science* **2020**, *1* (8), 100139. DOI: <a href="https://doi.org/10.1016/j.xcrp.2020.100139">https://doi.org/10.1016/j.xcrp.2020.100139</a>.
- (10) Lv, S.; Verhallen, T.; Vasileiadis, A.; Ooms, F.; Xu, Y.; Li, Z.; Li, Z.; Wagemaker, M. Operando monitoring the lithium spatial distribution of lithium metal anodes. *Nature Communications* **2018**, *9* (1), 2152. DOI: https://doi.org/10.1038/s41467-018-04394-3.
- (11) Leenheer, A. J.; Jungjohann, K. L.; Zavadil, K. R.; Sullivan, J. P.; Harris, C. T. Lithium Electrodeposition Dynamics in Aprotic Electrolyte Observed in Situ via Transmission Electron Microscopy. *ACS Nano* **2015**, *9* (4), 4379-4389. DOI: https://doi.org/10.1021/acsnano.5b00876.

- (12) Kushima, A.; So, K. P.; Su, C.; Bai, P.; Kuriyama, N.; Maebashi, T.; Fujiwara, Y.; Bazant, M. Z.; Li, J. Liquid cell transmission electron microscopy observation of lithium metal growth and dissolution: Root growth, dead lithium and lithium flotsams. *Nano Energy* **2017**, *32*, 271-279. DOI: https://doi.org/10.1016/j.nanoen.2016.12.001.
- (13) Chen, X.-R.; Yan, C.; Ding, J.-F.; Peng, H.-J.; Zhang, Q. New insights into "dead lithium" during stripping in lithium metal batteries. *Journal of Energy Chemistry* **2021**, *62*, 289-294. DOI: <a href="https://doi.org/10.1016/j.jechem.2021.03.048">https://doi.org/10.1016/j.jechem.2021.03.048</a>.
- (14) Bai, P.; Li, J.; Brushett, F. R.; Bazant, M. Z. Transition of lithium growth mechanisms in liquid electrolytes. *Energy & Environmental Science* **2016**, *9* (10), 3221-3229. DOI: https://doi.org/10.1039/C6EE01674J.
- (15) Li, S.; Fan, L.; Lu, Y. Rational design of robust-flexible protective layer for safe lithium metal battery. *Energy Storage Materials* **2019**, *18*, 205-212. DOI: https://doi.org/10.1016/j.ensm.2018.09.015.
- (16) Fan, L.; Sun, B.; Yan, K.; Xiong, P.; Guo, X.; Guo, Z.; Zhang, N.; Feng, Y.; Sun, K.; Wang, G. A Dual-Protective Artificial Interface for Stable Lithium Metal Anodes. *Advanced Energy Materials* **2021**, *11* (48), 2102242. DOI: <a href="https://doi.org/10.1002/aenm.202102242">https://doi.org/10.1002/aenm.202102242</a>.
- (17) Jin, C.; Liu, T.; Sheng, O.; Li, M.; Liu, T.; Yuan, Y.; Nai, J.; Ju, Z.; Zhang, W.; Liu, Y.; Wang, Y.; Lin, Z.; Lu, J.; Tao, X. Rejuvenating dead lithium supply in lithium metal anodes by iodine redox. *Nature Energy* **2021**, *6* (4), 378-387. DOI: https://doi.org/10.1038/s41560-021-00789-7.
- (18) Zhang, S.; Cheng, B.; Fang, Y.; Dang, D.; Shen, X.; Li, Z.; Wu, M.; Hong, Y.; Liu, Q. Inhibition of lithium dendrites and dead lithium by an ionic liquid additive toward safe and stable lithium metal anodes. *Chinese Chemical Letters* **2022**, *33* (8), 3951-3954. DOI: <a href="https://doi.org/10.1016/j.cclet.2021.11.024">https://doi.org/10.1016/j.cclet.2021.11.024</a>.
- (19) Zhang, Y.; Liu, J.; Li, Y.; Zhao, D.; Huang, W.; Zheng, Y.; Zhou, J.; Zhu, C.; Deng, C.; Sun, Y.; Qian, T.; Yan, C. Reactivating the Dead Lithium by Redox Shuttle to Promote the Efficient Utilization of Lithium for Anode Free Lithium Metal Batteries. *Advanced Functional Materials* **2023**, *33* (40), 2301332. DOI: <a href="https://doi.org/10.1002/adfm.202301332">https://doi.org/10.1002/adfm.202301332</a>.
- (20) Lee, J.; Choi, S. H.; Qutaish, H.; Hyeon, Y.; Han, S. A.; Heo, Y.-U.; Whang, D.; Lee, J.-W.; Moon, J.; Park, M.-S.; Kim, J. H.; Dou, S. X. Structurally stabilized lithium-metal anode via surface chemistry engineering. *Energy Storage Materials* **2021**, *37*, 315-324. DOI: https://doi.org/10.1016/j.ensm.2021.02.019.
- (21) Dachraoui, W.; Kühnel, R.-S.; Battaglia, C.; Erni, R. Nucleation, growth and dissolution of Li metal dendrites and the formation of dead Li in Li-ion batteries investigated by operando electrochemical liquid cell scanning transmission electron microscopy. *Nano Energy* **2024**, *130*, 110086. DOI: <a href="https://doi.org/10.1016/j.nanoen.2024.110086">https://doi.org/10.1016/j.nanoen.2024.110086</a>.
- (22) Fang, C.; Li, J.; Zhang, M.; Zhang, Y.; Yang, F.; Lee, J. Z.; Lee, M.-H.; Alvarado, J.; Schroeder, M. A.; Yang, Y.; Lu, B.; Williams, N.; Ceja, M.; Yang, L.; Cai, M.; Gu, J.; Xu, K.; Wang, X.; Meng, Y. S. Quantifying inactive lithium in lithium metal batteries. *Nature* **2019**, *572* (7770), 511-515. DOI: https://doi.org/10.1038/s41586-019-1481-z.

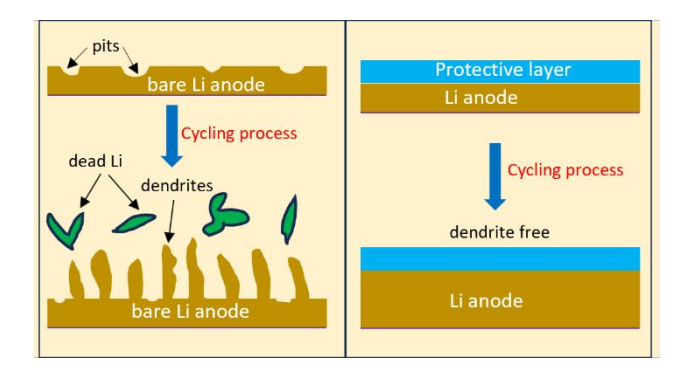
- (23) Zhang, K.; Wu, F.; Zhang, K.; Weng, S.; Wang, X.; Gao, M.; Sun, Y.; Cao, D.; Bai, Y.; Xu, H.; Wang, X.; Wu, C. Chlorinated dual-protective layers as interfacial stabilizer for dendrite-free lithium metal anode. *Energy Storage Materials* **2021**, *41*, 485-494. DOI: <a href="https://doi.org/10.1016/j.ensm.2021.06.023">https://doi.org/10.1016/j.ensm.2021.06.023</a>.
- (24) Liu, S.; Xia, X.; Deng, S.; Xie, D.; Yao, Z.; Zhang, L.; Zhang, S.; Wang, X.; Tu, J. In Situ Solid Electrolyte Interphase from Spray Quenching on Molten Li: A New Way to Construct High-Performance Lithium-Metal Anodes. *Advanced Materials* **2019**, *31* (3), 1806470. DOI: https://doi.org/10.1002/adma.201806470.
- (25) Monroe, C.; Newman, J. Dendrite Growth in Lithium/Polymer Systems: A Propagation Model for Liquid Electrolytes under Galvanostatic Conditions. *Journal of The Electrochemical Society* **2003**, *150* (10), A1377. DOI: https://doi.org/10.1149/1.1606686.
- (26) Guyer, J. E.; Boettinger, W. J.; Warren, J. A.; McFadden, G. B. Phase field modeling of electrochemistry. I. Equilibrium. *Physical Review E* **2004**, *69* (2), 021603. DOI: https://doi.org/10.1103/PhysRevE.69.021603.
- (27) Guyer, J. E.; Boettinger, W. J.; Warren, J. A.; McFadden, G. B. Phase field modeling of electrochemistry. II. Kinetics. *Physical Review E* **2004**, *69* (2), 021604. DOI: https://doi.org/10.1103/PhysRevE.69.021604.
- (28) Liang, L.; Qi, Y.; Xue, F.; Bhattacharya, S.; Harris, S. J.; Chen, L.-Q. Nonlinear phase-field model for electrode-electrolyte interface evolution. *Physical Review E* **2012**, *86* (5), 051609. DOI: https://doi.org/10.1103/PhysRevE.86.051609.
- (29) Ren, Y.; Zhang, K.; Zhou, Y.; Cao, Y. Phase-Field Simulation and Machine Learning Study of the Effects of Elastic and Plastic Properties of Electrodes and Solid Polymer Electrolytes on the Suppression of Li Dendrite Growth. *ACS Applied Materials & Interfaces* **2022**, *14* (27), 30658-30671. DOI: https://doi.org/10.1021/acsami.2c03000.
- (30) Lee, H.; Kwak, T.; Lee, W.; Song, J.; Kim, D. Effect of surface topography on dendritic growth in lithium metal batteries. *Journal of Power Sources* **2022**, *552*, 232264. DOI: https://doi.org/10.1016/j.jpowsour.2022.232264.
- (31) Cao, D.; Zhang, K.; Li, W.; Zhang, Y.; Ji, T.; Zhao, X.; Cakmak, E.; Zhu, J.; Cao, Y.; Zhu, H. Nondestructively Visualizing and Understanding the Mechano-Electro-chemical Origins of "Soft Short" and "Creeping" in All-Solid-State Batteries. *Advanced Functional Materials* **2023**, *33*, 2307998. DOI: https://doi.org/10.1002/adfm.202307998.
- (32) Gao, L. T.; Lyu, Y.; Guo, Z.-S. External Pressure Affecting Dendrite Growth and Dissolution in Lithium Metal Batteries During Cycles. *ACS Applied Materials & Interfaces* **2023**, *15* (50), 58416-58428. DOI: https://doi.org/10.1021/acsami.3c13972.
- (33) Tantratian, K.; Yan, H.; Ellwood, K.; Harrison, E. T.; Chen, L. Unraveling the Li Penetration Mechanism in Polycrystalline Solid Electrolytes. *Advanced Energy Materials* **2021**, *11* (13), 2003417. DOI: <a href="https://doi.org/10.1002/aenm.202003417">https://doi.org/10.1002/aenm.202003417</a>.

- (34) Zhang, H.; Okur, F.; Pant, B.; Klimpel, M.; Butenko, S.; Karabay, D. T.; Parrilli, A.; Neels, A.; Cao, Y.; Kravchyk, K. V.; Kovalenko, M. V. Garnet-Based Solid-State Li Batteries with High-Surface-Area Porous LLZO Membranes. *ACS Applied Materials & Interfaces* **2024**, *16* (10), 12353-12362. DOI: https://doi.org/10.1021/acsami.3c14422.
- (35) Yan, H. H.; Bie, Y. H.; Cui, X. Y.; Xiong, G. P.; Chen, L. A computational investigation of thermal effect on lithium dendrite growth. *Energy Conversion and Management* **2018**, *161*, 193-204. DOI: <a href="https://doi.org/10.1016/j.enconman.2018.02.002">https://doi.org/10.1016/j.enconman.2018.02.002</a>.
- (36) Pant, B.; Ren, Y.; Cao, Y. Phase-Field Simulation of a Dynamic Protective Layer for the Inhibition of Dendrite Growth in Zinc Metal Batteries. *ACS Applied Materials & Interfaces* **2023**, *15* (51), 59329-59336. DOI: https://doi.org/10.1021/acsami.3c11936.
- (37) Li, G.; Liu, Z.; Wang, D.; He, X.; Liu, S.; Gao, Y.; AlZahrani, A.; Kim, S. H.; Chen, L.-Q.; Wang, D. Electrokinetic Phenomena Enhanced Lithium-Ion Transport in Leaky Film for Stable Lithium Metal Anodes. *Advanced Energy Materials* **2019**, *9* (22), 1900704, <a href="https://doi.org/10.1002/aenm.201900704">https://doi.org/10.1002/aenm.201900704</a>. DOI: <a href="https://doi.org/10.1002/aenm.201900704">https://doi.org/10.1002/aenm.201900704</a>.
- (38) Zhang, R.; Shen, X.; Zhang, Y.-T.; Zhong, X.-L.; Ju, H.-T.; Huang, T.-X.; Chen, X.; Zhang, J.-D.; Huang, J.-Q. Dead lithium formation in lithium metal batteries: A phase field model. *Journal of Energy Chemistry* **2022**, *71*, 29-35. DOI: https://doi.org/10.1016/j.jechem.2021.12.020.
- (39) Shen, X.; Zhang, R.; Shi, P.; Zhang, X.-Q.; Chen, X.; Zhao, C.-Z.; Wu, P.; Guo, Y.-M.; Huang, J.-Q.; Zhang, Q. The dead lithium formation under mechano-electrochemical coupling in lithium metal batteries. *Fundamental Research* **2022**. DOI: <a href="https://doi.org/10.1016/j.fmre.2022.11.005">https://doi.org/10.1016/j.fmre.2022.11.005</a>.
- (40) Ren, Y.; Zhou, Y.; Cao, Y. Inhibit of Lithium Dendrite Growth in Solid Composite Electrolyte by Phase-Field Modeling. *The Journal of Physical Chemistry C* **2020**, *124* (23), 12195-12204. DOI: https://doi.org/10.1021/acs.jpcc.0c01116.
- (41) Chen, L.; Zhang, H. W.; Liang, L. Y.; Liu, Z.; Qi, Y.; Lu, P.; Chen, J.; Chen, L.-Q. Modulation of dendritic patterns during electrodeposition: A nonlinear phase-field model. *Journal of Power Sources* **2015**, *300*, 376-385. DOI: https://doi.org/10.1016/j.jpowsour.2015.09.055.
- (42) Mirambell, E.; Real, E. On the calculation of deflections in structural stainless steel beams: an experimental and numerical investigation. *Journal of Constructional Steel Research* **2000**, *54* (1), 109-133. DOI: https://doi.org/10.1016/S0143-974X(99)00051-6.
- (43) Pokharel, J.; Cresce, A.; Pant, B.; Yang, M. Y.; Gurung, A.; He, W.; Baniya, A.; Lamsal, B. S.; Yang, Z.; Gent, S.; Xian, X.; Cao, Y.; Goddard, W. A.; Xu, K.; Zhou, Y. Manipulating the diffusion energy barrier at the lithium metal electrolyte interface for dendrite-free long-life batteries. *Nature Communications* **2024**, *15* (1), 3085. DOI: https://doi.org/10.1038/s41467-024-47521-z.
- (44) Liu, Y.; Xu, X.; Sadd, M.; Kapitanova, O. O.; Krivchenko, V. A.; Ban, J.; Wang, J.; Jiao, X.; Song, Z.; Song, J.; Xiong, S.; Matic, A. Insight into the Critical Role of Exchange Current Density on Electrodeposition Behavior of Lithium Metal. *Advanced Science* **2021**, *8* (5), 2003301. DOI: <a href="https://doi.org/10.1002/advs.202003301">https://doi.org/10.1002/advs.202003301</a>.

- (45) Guan, X.; Wang, A.; Liu, S.; Li, G.; Liang, F.; Yang, Y.-W.; Liu, X.; Luo, J. Controlling Nucleation in Lithium Metal Anodes. *Small* **2018**, *14* (37), 1801423. DOI: <a href="https://doi.org/10.1002/smll.201801423">https://doi.org/10.1002/smll.201801423</a>.
- (46) Zhang, X.; Wang, A.; Liu, X.; Luo, J. Dendrites in Lithium Metal Anodes: Suppression, Regulation, and Elimination. *Accounts of Chemical Research* **2019**, *52* (11), 3223-3232. DOI: https://doi.org/10.1021/acs.accounts.9b00437.
- (47) Qi, L.; Wu, Z.; Zhao, B.; Liu, B.; Wang, W.; Pei, H.; Dong, Y.; Zhang, S.; Yang, Z.; Qu, L.; Zhang, W. Advances in Artificial Layers for Stable Lithium Metal Anodes. *Chemistry A European Journal* **2020**, *26* (19), 4193-4203. DOI: https://doi.org/10.1002/chem.201904631.
- (48) Liu, H.; Cheng, X.-B.; Xu, R.; Zhang, X.-Q.; Yan, C.; Huang, J.-Q.; Zhang, Q. Plating/Stripping Behavior of Actual Lithium Metal Anode. *Advanced Energy Materials* **2019**, *9* (44), 1902254. DOI: https://doi.org/10.1002/aenm.201902254.
- (49) Lee, H. G.; Kim, S. Y.; Lee, J. S. Dynamic observation of dendrite growth on lithium metal anode during battery charging/discharging cycles. *npj Computational Materials* **2022**, *8* (1), 103. DOI: https://doi.org/10.1038/s41524-022-00788-6.
- (50) Yamaki, J.-i.; Tobishima, S.-i.; Hayashi, K.; Keiichi, S.; Nemoto, Y.; Arakawa, M. A consideration of the morphology of electrochemically deposited lithium in an organic electrolyte. *Journal of Power Sources* **1998**, *74* (2), 219-227. DOI: <a href="https://doi.org/10.1016/S0378-7753(98)00067-6">https://doi.org/10.1016/S0378-7753(98)00067-6</a>.
- (51) Fang, S.; Wu, F.; Zhao, S.; Zarrabeitia, M.; Kim, G.-T.; Kim, J.-K.; Zhou, N.; Passerini, S. Adaptive Multi-Site Gradient Adsorption of Siloxane-Based Protective Layers Enable High Performance Lithium-Metal Batteries. *Advanced Energy Materials* **2023**, *13* (46), 2302577. DOI: https://doi.org/10.1002/aenm.202302577.
- (52) Liu, F.; Wang, L.; Zhang, Z.; Shi, P.; Feng, Y.; Yao, Y.; Ye, S.; Wang, H.; Wu, X.; Yu, Y. A Mixed Lithium-Ion Conductive Li2S/Li2Se Protection Layer for Stable Lithium Metal Anode. *Advanced Functional Materials* **2020**, *30* (23), 2001607. DOI: <a href="https://doi.org/10.1002/adfm.202001607">https://doi.org/10.1002/adfm.202001607</a>.
- (53) Chen, K.; Pathak, R.; Gurung, A.; Adhamash, E. A.; Bahrami, B.; He, Q.; Qiao, H.; Smirnova, A. L.; Wu, J. J.; Qiao, Q.; Zhou, Y. Flower-shaped lithium nitride as a protective layer via facile plasma activation for stable lithium metal anodes. *Energy Storage Materials* **2019**, *18*, 389-396. DOI: https://doi.org/10.1016/j.ensm.2019.02.006.
- (54) Jo, H.; Song, D.; Jeong, Y.-C.; Lee, Y. M.; Ryou, M.-H. Study on dead-Li suppression mechanism of Lihosting vapor-grown-carbon-nanofiber-based protective layer for Li metal anodes. *Journal of Power Sources* **2019**, *409*, 132-138. DOI: <a href="https://doi.org/10.1016/j.jpowsour.2018.09.059">https://doi.org/10.1016/j.jpowsour.2018.09.059</a>.
- (55) Sun, J.; Zhang, S.; Li, J.; Xie, B.; Ma, J.; Dong, S.; Cui, G. Robust Transport: An Artificial Solid Electrolyte Interphase Design for Anode-Free Lithium-Metal Batteries. *Advanced Materials* **2023**, *35* (20), 2209404. DOI: <a href="https://doi.org/10.1002/adma.202209404">https://doi.org/10.1002/adma.202209404</a>.
- (56) Xie, J.; Wang, J.; Lee, H. R.; Yan, K.; Li, Y.; Shi, F.; Huang, W.; Pei, A.; Chen, G.; Subbaraman, R.; Christensen, J.; Cui, Y. Engineering stable interfaces for three-dimensional lithium metal anodes. *Science Advances* **2018**, *4* (7), eaat5168. DOI: https://doi.org/10.1126/sciadv.aat5168.

(57) Bieker, G.; Winter, M.; Bieker, P. Electrochemical in situ investigations of SEI and dendrite formation on the lithium metal anode. *Physical Chemistry Chemical Physics* **2015**, *17* (14), 8670-8679, 10.1039/C4CP05865H. DOI: https://doi.org/10.1039/C4CP05865H.

(58) Wu, B.; Lochala, J.; Taverne, T.; Xiao, J. The interplay between solid electrolyte interface (SEI) and dendritic lithium growth. *Nano Energy* **2017**, *40*, 34-41. DOI: https://doi.org/10.1016/j.nanoen.2017.08.005.



For table of content only.